



## Biochemomechanical Tensegrity Model of Cytoskeletons

Shu-Yi Sun <sup>a</sup>, Li-Yuan Zhang <sup>b</sup>, Xindong Chen <sup>a</sup>, Xi-Qiao Feng <sup>a,c,\*</sup>

<sup>a</sup> Institute of Biomechanics and Medical Engineering, AML, Department of Engineering Mechanics, Tsinghua University, Beijing, 100084, China

<sup>b</sup> School of Mechanical Engineering, University of Science and Technology Beijing, Beijing, 100083, China

<sup>c</sup> State Key Laboratory of Tribology in Advanced Equipment (SKLT), Tsinghua University, Beijing, 100084, China



### ARTICLE INFO

**Keywords:**

Cytoskeleton  
Tensegrity  
Biochemomechanical coupling  
Cell oscillation  
Dynamic behavior

### ABSTRACT

Active deformation and remodeling of cytoskeletons play a key role in many physiological and pathological dynamic processes such as embryonic development, regulation of the epigenetic state, and cancer invasion. However, it remains unclear how such molecular mechanisms as the polymerization and depolymerization of actin and microtubular networks, the motion of motors, and the regulation of upstream molecular signals coordinate the dynamic behaviors of cells. In this paper, we establish a biochemomechanical tensegrity model of cytoskeletons to investigate the spatiotemporal dynamics of cells. The reaction and diffusion of biochemical factors, the active contraction of actomyosin filaments, and mechanical-chemical feedback mechanisms are considered in this model. Instability analysis is performed to capture the dominant features of the active behaviors of cytoskeletons and scrutinize the role of mechanical-chemical feedback in the dynamic state transitions. Then, this model is applied to analyze the complicated processes spanning from the dynamic behaviors of an actomyosin string to the periodic cellular oscillations, which are pivotal for embryonic development and cancer invasion. It is revealed that the interplay of internal active forces and chemical reactions may induce spontaneous oscillations of cells. The results agree well with relevant experimental measurements. This work provides not only a theoretical framework for studying the multiscale biochemomechanical coupling behaviors of cytoskeletons but also a tool for simulating the spatiotemporal dynamics of cells under various physiological and pathological conditions.

### 1. Introduction

Mechanical forces sculpt life at all length scales, from biomolecules, cells, tissues, organs, to the whole body (Dance, 2021). At the subcellular scale, cytoskeletons, assembled by a variety of biopolymer filaments, provide a structural basis and a scaffold for the mechanical and morphologic behaviors of cells. During embryonic development (Valet et al., 2022) and cancer invasion (Bera et al., 2022), for example, the cytoskeleton senses and transmits forces to interact with the adjacent cells and extracellular environment, with the assistance of transmembrane receptor proteins. Meanwhile, energy-consuming molecular motors in the cytoskeleton drive the relative sliding of filaments to generate active contractile forces. Continuous polymerization and depolymerization of biopolymer filaments endow the cytoskeleton with highly dynamic features (Gong et al., 2019). Thereby, cytoskeletons, composed of different kinds of molecular proteins, can self-organize into greatly diverse structures and preserve long-range order to achieve various dynamic functions of cells (Huber et al., 2013).

\* Corresponding author

E-mail address: [fengxq@tsinghua.edu.cn](mailto:fengxq@tsinghua.edu.cn) (X.-Q. Feng).

The multiple functions of a cytoskeleton rely on the complicated interplay of mechanical, chemical, and biological cues between cytoskeletal proteins. Mechanical signals can stimulate biochemical signal pathways, which, in turn, can adapt the generation, transmission, and reception of mechanical signals (Sun et al., 2022). On one hand, the cytoskeleton converts the perceived forces into the programs of chemical reactions and gene expressions. For example, mechanical stretches activate membrane channels (e.g., Piezo1) and influence calcium ion-related signaling proteins (Gudipaty et al., 2017). In response to stresses, Rho family proteins adjust the active force generation in the cytoskeleton by regulating myosin-II activity and the polymerization of actin filament (F-actin) (Lessey et al., 2012), and thus regulate cell migrations (Bera et al., 2022). Cytoskeleton-induced nuclear deformation can prime the epigenetic state and promote cell reprogramming (Song et al., 2022). In addition, transmembrane proteins usually sense the cell surface curvature, which is determined by cytoskeleton protrusions, to organize biochemical reactions in a spatiotemporal manner (Antonny, 2011). On the other hand, the mechano-triggered biochemical programs, in turn, adjust the architecture and force generation of the cytoskeleton. For example, lamellipodial branched actin networks can adapt the F-actin densities and propulsive forces based on extracellular matrix (ECM) resistance (Chen et al., 2020; Mueller et al., 2017). Through this kind of biochemomechanical coupling feedback loop, cells possess a powerful and versatile capability to deal with complex extracellular environments and thus to ensure the accomplishments of their biological functions. There are mainly three types of biopolymer filaments in the cytoskeleton, i.e., F-actins, intermediate filaments, and microtubules, each of which is assembled by a large number of individual monomers. The dynamic self-assembly of the biopolymer filaments (Fletcher and Mullins, 2010), which are regulated by the biochemical reactions in the cell body and multi-field loads from the extracellular matrix and neighboring cells, adapts the macroscopic mechanical properties and micromorphology of the cytoskeleton. In particular, the orientation and distribution of stress fibers and microtubule structures change and harmonize with cellular activities and the surroundings evidently (Théry, 2010; Wang et al., 2017; Zhang et al., 2014a). In complex environments, such as a 3D ECM or viscoelastic soft substrate, cytoskeleton-based propulsive forces drive cell morphogenesis, migrations, and oscillations (Adebawale et al., 2021; Lee et al., 2021; Reversat et al., 2020). Through these processes, cells can perceive mechanical stimuli accurately and then adapt themselves to varying mechanical microenvironments to perform their functions.

Theoretical and numerical efforts have been directed toward modeling the dynamics of a cytoskeleton according to its structures and functions at different length scales (Sun et al., 2022). Among others, molecular dynamics methods have been used to study monomeric actin and polymeric networks by tracking the motions of constituent components as an ensemble of atoms, molecules, or particles with specified potential energies (Dalheimer et al., 2008; Gong et al., 2019). To investigate the force generation in living cells, the constitutive relation of a single F-actin was constructed by accounting for the dynamic reorganization of the cytoskeleton (Deshpande et al., 2007). The constitutive relations of F-actin and crosslinking proteins have been derived theoretically and used to predict the mechanical properties of actin networks (Deshpande et al., 2008; Ferreira et al., 2018; Lopez-Menendez and Gonzalez-Torres, 2019; Wang et al., 2020). Especially, a multiscale model of lamellipodial actin networks was developed by considering the mechano-chemical assembling and disassembling processes of different intracellular proteins, such as F-actin, Arp2/3 complex, filamin-A,  $\alpha$ -actinin, and capping proteins (Chen et al., 2020). This model revealed how these proteins regulate the elastic properties of a lamellipodial actin network and cell migration. Furthermore, the dynamic behaviors of the cytoskeleton have been implemented into the continuum mechanics models of fluids or solids by considering its active forces or deformations (Goriely, 2018; Marchetti et al., 2013; Salbreux and Jülicher, 2017; Shao et al., 2012; Yang et al., 2023). These models also show good performance in simulating the migration, polarization, and some other dynamic processes of cells with the effects of mechanical forces.

In the recent years, the biochemomechanical coupling mechanisms underlying the generation of active forces and structural evolutions have attracted considerable attention. For example, Besser and Schwarz (2007) described the activation of myosin-II molecular motors through the Rho-pathway by implementing a system of reaction–diffusion equations into a viscoelastic and contractile stress fiber model. A chemical kinetic model was proposed to describe the mechanochemical response of force generation in smooth muscles, in which calcium-dependent myosin phosphorylation was regarded as a regulatory mechanism (Murtada et al., 2010). Recho et al. (2019) coupled the morphogen concentrations with extracellular fluid flows in a two-phase poroelastic rheology model and, thereby, proposed non-Turing mechanisms for the formation of spatial patterns in tissues. Lin et al. (2017) integrated the Rho-effector signaling pathway, which is responsible for the activation of myosin-II molecular motor and the cell contractility, into the dynamic vertex model to investigate the collective oscillations in a confluent cell monolayer. The interplay between the cellular active deformations and the activities of chemical factors was described by a set of chemomechanical coupling dynamic equations (Lin et al., 2018). Yin et al. (2021, 2022) presented a generic active solid shell theory for modeling living thin structures such as cell cortex layers and multicellular sheets, emphasizing the important role of mechanical feedback in biochemical fields in the morphogenesis of cellular patterns. These works provide an exemplary framework for modeling the biochemomechanical coupling relationship of the cytoskeleton.

Prestresses in the structural elements of a cytoskeleton are crucial for its multiple functions and structural stability. Specifically, the active contractile stresses in the cytoskeleton interact with the extracellular microenvironments and contribute to the dynamic behaviors of the cell. The cytoskeletal filaments in living cells can bear significant tensile and compressive forces, which share a high similarity to tensegrity structures, a building system consisting of connected string and bar elements (Wang et al., 2009). Therefore, the tensegrity model has been proposed to investigate the mechanical properties of cytoskeletons and to explain how cells coordinate their deformations, motions, and functions through the rearrangement of cytoskeletal filament networks (Ingber et al., 2014; Wang et al., 2001; Zhang et al., 2017). This model can elucidate various experimental phenomena of cells and highlight the significance of mechanical forces in regulating biological functions (Coughlin and Stamenović, 1998; Wang et al., 1993; Wang et al., 2001; Xu et al., 2018). For example, the spatiotemporal dynamics of collective cells in an epithelial monolayer has been studied by using a group of connected tensegrity structures (Liu et al., 2021; Wang and Xu, 2022). Both physiological and pathological behaviors of cells are tightly dependent on the coupling interplay between mechanical forces and biochemical cues. However, the previous tensegrity

models have limited applicability when it comes to examining the complex biochemomechanical coupling processes of living cells (Ingber, 2018; Ingber et al., 2014). As the cytoskeletal active stresses generated by molecular motors are dominated by biochemical responses to mechanical factors, a biochemomechanical model is desired to explore the spatiotemporal evolutions of cells that involve interactions of different molecular proteins.

In this paper, we establish a tensegrity theory for a cytoskeleton by considering its biochemomechanical coupling mechanisms. This model can be used to investigate various dynamic behaviors of cells, such as deformation, motion, migration, and oscillation, during embryonic development, regulation of the epigenetic state, and cancer invasion. This paper is outlined as follows. In Section 2, we formulate the biochemomechanical tensegrity model. In Section 3, numerical schemes are given to solve the dynamic evolutions of the mechanical and chemical fields, including chemical diffusion among the elements and the form finding of tensegrity. In Section 4, linear stability analysis for an actomyosin string is performed to scrutinize the biochemomechanical regulation of the dynamic behaviors of cytoskeletons. In Section 5, we further provide illustrative numerical examples of an actomyosin string and the oscillatory patterns in a single cell. The roles of the feedback mechanisms in the dynamic state transitions are also discussed through the combination of stability phase diagrams and direct simulations. Section 6 summarizes the main conclusions drawn from this study.

## 2. Biochemomechanical tensegrity model

### 2.1. Tensegrity model of cytoskeleton

In the cytoskeleton of a living cell, the actin stress fibers are tensionally prestressed (Imtiaz et al., 2006; Kumar et al., 2006) while the microtubules are mainly subjected to compression (Brangwynne et al., 2006). This load-bearing feature is reminiscent of tensegrity structures in which a continuous series of tensile string elements are outstretched by isolated compression-resistant bar elements to maintain the structural equilibrium and stability (Ingber, 2018). Therefore, we here model a cytoskeleton (Fig. 1(a) and (b)) as a tensegrity structure (Fig. 1(c)), consisting of a series of connected strings (actin cortex and stress fibers) and bars (microtubules and stiffened cross-linked actin bundles). A biochemomechanical coupling tensegrity theory will be formulated below by considering the biochemical mechanisms that influence the deformation behaviors of the string and bar elements in the cytoskeleton. This model will be used to investigate the dynamic behaviors of cells, e.g., deformation, migration, and oscillation.

More specifically, the actin cortex and stress fibers are modeled as a continuous series of string elements that can only bear axial

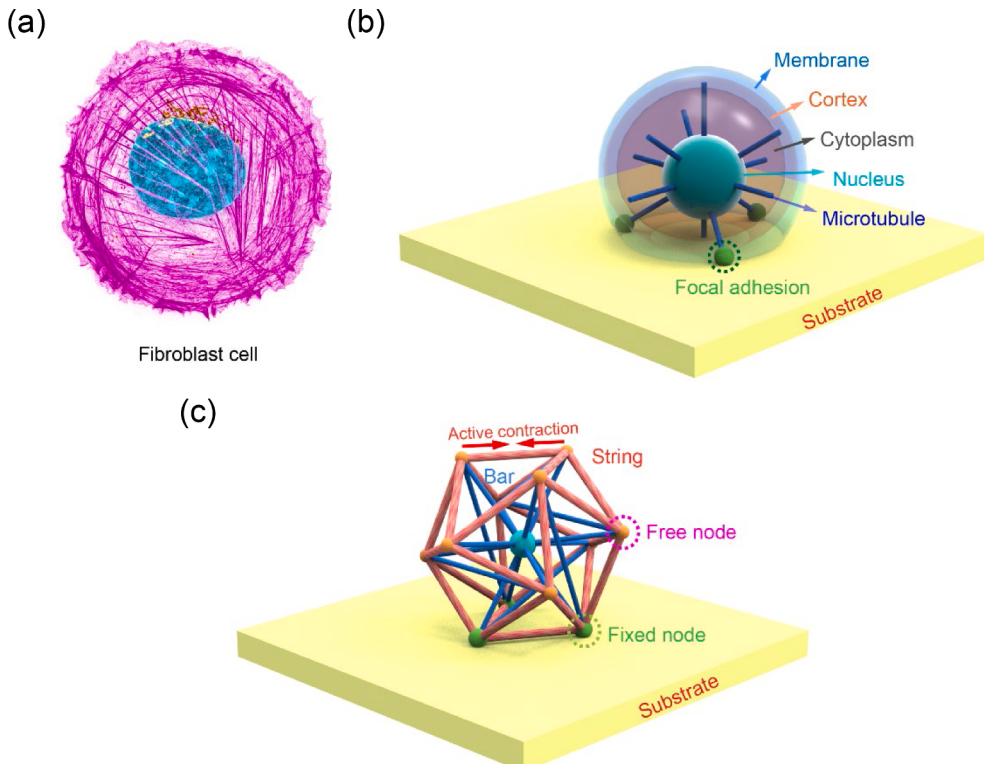


**Fig. 1.** (a) Photomicrograph of a fibroblast cell stained for actin (magenta), golgi (yellow), and nucleus (blue). The actin arrangement shows dense F-actin in the cortex. The photo is adapted from Fenix and Burnette (2018). (b) Schematic of the architecture of a fibroblast cell adhered to a substrate. The cortex (red) is tensionally prestressed and the microtubules (blue) are mainly subjected to compression. (c) Schematic of the tensegrity model of cytoskeleton. The strings (red) are prestressed and can contract actively.

tensile forces. In response to the external mechanical and chemical stimuli, these strings can contract actively and thereby generate active forces. Microtubules and stiffened cross-linked actin bundles are modeled as bar elements that can withstand both axial tensile and compressive forces. The bars can elongate or shrink spontaneously, which plays a significant role in many dynamic processes of cells, e.g., cellular shape evolution and protrusion. The strings and bars are connected together by nodes, which can not only bridge the internal forces in all elements but also describe the intercellular and cell–substrate adhesion by introducing the displacement constraints and external forces at some nodes.

The dynamics of a cytoskeleton is regulated by a variety of biochemical cues, such as nucleation-promoting factors, capping proteins, depolymerizing factors, severing factors, and crosslinkers (Fletcher and Mullins, 2010). By correlating the deformations of the strings and bars with these biochemical cues, we develop a biochemomechanical tensegrity model that incorporates the biochemomechanical coupling regulation. In general, the spatial distributions of the biochemical factors are not uniform in a cell but depend on their diffusion, convection, reaction consumption and production. Therefore, we will calculate their spatial concentrations in elements of the tensegrity by using the reaction–diffusion equations of biochemical factors. In the biochemomechanical tensegrity model, the mechanical properties and lengths of the string and bar elements are regulated by the evolutions of the chemical concentrations, which are coupled with mechanical and geometric variables according to the biochemomechanical feedback mechanisms. In what follows, we will formulate this biochemomechanical coupling tensegrity theory.

### 2.1.1. Equilibrium equations

The cytoskeleton is modeled as a tensegrity with  $n_e = n_b + n_s$  elements, including  $n_s$  strings and  $n_b$  bars connected by  $n_n$  nodes. Refer to a three-dimensional Cartesian coordinate system, as shown in Fig. 2. Let  $\mathbf{p}_i = [x_i, y_i, z_i]^T$  and  $\mathbf{f}_i = [f_{x,i}, f_{y,i}, f_{z,i}]^T$  denote the coordinate vector and the force vector of node  $i$  ( $i = 1, 2, \dots, n_n$ ), respectively. We use the subscript  $e(ij)$  to indicate the element connecting nodes  $i$  and  $j$ . The length, natural length, internal force, and axial stiffness of the element  $e(ij)$  are denoted as  $l_{e(ij)}$ ,  $l_{n,e(ij)}$ ,  $t_{e(ij)}$ , and  $g_{e(ij)}$ , respectively, and its direction vector is  $(\mathbf{p}_i - \mathbf{p}_j)/l_{e(ij)}$ .

At each node  $i$  ( $i = 1, 2, \dots, n_n$ ), the forces in the bar and string elements satisfy the equilibrium condition (Zhang et al., 2013)

$$\sum_j \frac{\mathbf{p}_i - \mathbf{p}_j}{l_{e(ij)}} t_{e(ij)} = \mathbf{f}_i, \quad (1)$$

where the index  $j$  denotes all nodes connected to node  $i$ , as shown in Fig. 2.

The equilibrium condition at all nodes can be integrated into the matrix form (Zhang et al., 2013),

$$\mathbf{A} \cdot \mathbf{t} = \mathbf{f}, \quad (2)$$

where  $\mathbf{A} \in \mathbb{R}^{3n_n \times n_e}$  is the equilibrium matrix constructed by the direction vectors of all elements,  $\mathbf{t} = [\dots, t_{e(ij)}, \dots]^T \in \mathbb{R}^{n_e}$  contains the internal forces of all elements, and  $\mathbf{f} = [\dots, \mathbf{f}_i^T, \dots]^T \in \mathbb{R}^{3n_n}$  contains the external force components of all nodes. The equilibrium condition in Eq. (2) provides the relation between the internal forces in all elements and the external forces at the nodes.

In terms of the force density  $q_{e(ij)} = t_{e(ij)}/l_{e(ij)}$  in element  $e(ij)$ , the equilibrium condition in Eq. (1) can be re-expressed as

$$\sum_j q_{e(ij)} (\mathbf{p}_i - \mathbf{p}_j) = \mathbf{f}_i, \quad (3)$$

which enables us to more easily determine the changes of the external forces with respect to the nodal displacements. Similarly to Eq.

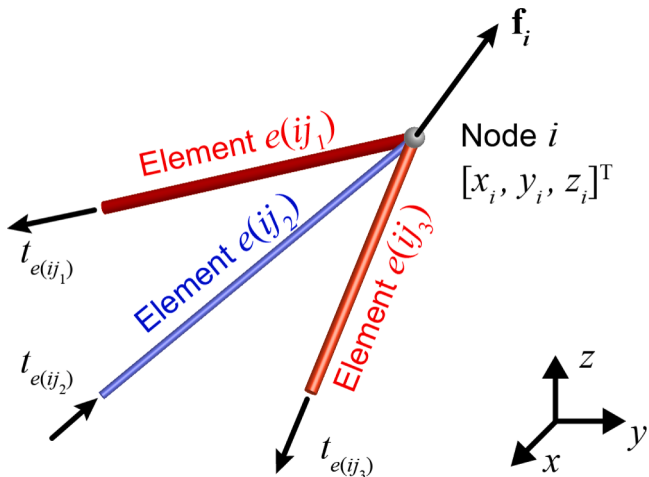


**Fig. 2.** Equilibrium between the internal forces and the externally applied force at node  $i$ .

(2), the matrix form of Eq. (3) is (Zhang et al., 2013)

$$\mathbf{S} \cdot \mathbf{p} = \mathbf{f}, \quad (4)$$

where  $\mathbf{p} = [\dots, \mathbf{p}_i^T, \dots]^T \in \mathbb{R}^{3n_a}$  contains the coordinate components of all nodes. Eq. (4) gives the dependence of the nodal external forces on the nodal coordinates.  $\mathbf{S} \in \mathbb{R}^{3n_a \times 3n_a}$  denotes the stress matrix, which can be obtained by reshaping the Kronecker product  $(\mathbf{C}^T \cdot \mathbf{Q} \cdot \mathbf{C}) \otimes \mathbf{I}$ , where  $\mathbf{Q} = \text{diag}(\dots, q_{e(ij)}, \dots) \in \mathbb{R}^{n_c \times n_c}$  is a diagonal matrix constructed by the force densities of all elements,  $\mathbf{I}$  is the second-order identity tensor, and  $\mathbf{C} \in \mathbb{R}^{n_c \times n_a}$  is the connection matrix defined by

$$C_{ij} = \begin{cases} 1, & \text{if node } j \text{ is the first node of element } i, \\ -1, & \text{if node } j \text{ is the second node of element } i, \\ 0, & \text{other cases,} \end{cases} \quad (5)$$

which specifies the connection relationship of the nodes and the elements.

### 2.1.2. Kinematic equations

The kinematic equation of a tensegrity, which connects the nodal coordinates with the element lengths, is used to track its mechanical response to loading. The length of the element  $e(ij)$  can be expressed as

$$l_{e(ij)} = |\mathbf{p}_i - \mathbf{p}_j|. \quad (6)$$

We define the element length vector  $\mathbf{l} = [\dots, l_{e(ij)}, \dots]^T \in \mathbb{R}^{n_c}$ . Then the incremental kinematic equations can be written as (Zhang et al., 2013)

$$\delta \mathbf{l} = \mathbf{B} \cdot \delta \mathbf{p}, \quad (7)$$

where  $\delta$  denotes the increment of the corresponding variable. The coefficient matrix  $\mathbf{B}$  can be obtained by using the virtual work principle on the equilibrium matrix in Eq. (2). Thus, Eq. (7) becomes

$$\delta \mathbf{l} = \mathbf{A}^T \cdot \delta \mathbf{p}, \quad (8)$$

which can also be used in the cases of nonlinear elements (Zhang et al., 2013).

### 2.1.3. Constitutive laws

We assume that all elements in the tensegrity have uniform and elastic constitutive relations but their mechanical properties and lengths are regulated by the biochemical feedback mechanisms. The viscous properties of the string and bar elements can also be implemented into the model but are omitted in this work for simplicity.

The nonlinear constitutive relation of a bar can be expressed as (Zhang et al., 2013)

$$t_{e(ij)} = \int_{l_{n,e(ij)}}^{l_{e(ij)}} g_{e(ij)}(\xi) d\xi, \quad (9)$$

where the axial stiffness  $g_{e(ij)}(\xi)$  is a function of the current length  $\xi$ . For a string element that cannot withstand compression, the constitutive relation in Eq. (9) is modified as

$$t_{e(ij)} = \begin{cases} \int_{l_{n,e(ij)}}^{l_{e(ij)}} g_{e(ij)}(\xi) d\xi, & l_{e(ij)} > l_{n,e(ij)}, \\ 0, & l_{e(ij)} \leq l_{n,e(ij)}. \end{cases} \quad (10)$$

If all elements are linearly elastic, Eqs. (9) and (10) reduce to

$$t_{e(ij)} = g_{e(ij)} [l_{e(ij)} - l_{n,e(ij)}], \quad (11)$$

$$t_{e(ij)} = \begin{cases} g_{e(ij)} [l_{e(ij)} - l_{n,e(ij)}], & l_{e(ij)} > l_{n,e(ij)}, \\ 0, & l_{e(ij)} \leq l_{n,e(ij)}, \end{cases} \quad (12)$$

respectively. Integrating the constitutive relation of all elements, we obtain

$$\delta \mathbf{t} = \mathbf{G} \cdot \delta \mathbf{l}, \quad (13)$$

where  $\mathbf{G} = \text{diag}(\dots, g_{e(ij)}, \dots) \in \mathbb{R}^{n_c \times n_c}$  is the stiffness matrix of the whole tensegrity structure. If a string is slack, the corresponding diagonal component  $g_{e(ij)}$  will be zero.

## 2.2. Biochemical regulation mechanisms

In general, the active cellular behaviors are jointly driven by two kinds of cytoskeletal forces, *i.e.*, contractile force and propulsive force. The energy-consuming molecular motors, myosin-II, generate active contraction of F-actin network in the cytoskeleton (Murrell et al., 2015). The polymerization growth of cytoskeletal filaments produces propulsive forces to form protrusion structures or sustain cell morphology in highly varying ECMs (Inagaki and Katsuno, 2017). RhoA, a small GTPase protein of Rho family, is one main upstream signal of myosin-II activity and F-actin polymerization (Lecuit et al., 2011; Lessey et al., 2012). In the present work, therefore, we will mainly examine how the RhoA-effector signaling pathway regulates the dynamics of a cytoskeleton (Lessey et al., 2012; Miller and Davidson, 2013). Other signaling pathways (*e.g.*, Rho1 and  $\text{Ca}^{2+}$ ) can also be taken into account similarly (Munjal et al., 2015; Salbreux et al., 2007; Shenoy et al., 2016).

### 2.2.1. Active force generation in strings

Actin monomers self-assemble into polarized F-actins, which have a growing barbed end and a vanishing pointed end (the rear) (Inagaki and Katsuno, 2017). F-actin chains can be attached by myosin molecules, which drive the sliding of bonded anti-parallel F-actins with respect to each other (Koenderink and Paluch, 2018). The strain mismatch of the F-actin chains engendered in this process exerts an active contraction force (Yin et al., 2021). Therefore, the activation of myosin-II and the polymerization of F-actin promote the contraction of the cytoskeleton. It has been found that the activation of RhoA promotes phosphorylation of myosin light chains (MLCs) and thus enhances myosin-II activity (Lessey et al., 2012). In addition, the activation of RhoA also accelerates the polymerization of F-actin, and finally promotes the cytoskeleton contraction together with myosin activation. In turn, the contraction of F-actin chains will down-regulate the activation of RhoA, preventing their further contraction (Bischof et al., 2017). This negative feedback mechanism is significant for the adaption of cortical contractility to the variations in the cell size and geometry, and the mechanical microenvironment as well.

On the basis of the above findings, we here adopt a negative feedback loop, as shown in Fig. 3(a), to represent the biochemomechanical coupling mechanisms in the tensegrity model of cytoskeleton (Yin et al., 2021). This biochemomechanical feedback regulates the active force generation in the strings. The normalized concentration of GTP-binding active RhoA (RhoA-GTP), denoted as  $C_R$ , is introduced to quantify the RhoA activation level, and the normalized concentration of actomyosin, denoted as  $C_A$ , stands for the level of MLC phosphorylation and F-actin polymerization. The evolutions of the biochemical factors in element  $e(ij)$ ,  $C_{R,e(ij)}$  and  $C_{A,e(ij)}$ , are described by the following modified reaction-diffusion equations with mechanical feedback effects (Yin et al., 2021),

$$\frac{dC_{R,e(ij)}}{dt} = D_R \Delta_T C_{R,e(ij)} + k_R^{\text{on}} \frac{C_{R,e(ij)}^n}{K_R^n + C_{R,e(ij)}^n} (1 - C_{R,e(ij)}) - k_R^{\text{off}} C_{R,e(ij)} - k_m^{\text{off}} f(\lambda_{e(ij)}) C_{R,e(ij)}, \quad (14)$$

$$\frac{dC_{A,e(ij)}}{dt} = D_A \Delta_T C_{A,e(ij)} + k_A^{\text{on}} \frac{C_{R,e(ij)}^n}{K_A^n + C_{R,e(ij)}^n} (1 - C_{A,e(ij)}) - k_A^{\text{off}} C_{A,e(ij)}, \quad (15)$$

where the subscripts R and A indicate RhoA-GTP and actomyosin, respectively. The first items on the right-hand sides of Eqs. (14) and (15) describe the diffusion of biochemical factors in the cytoskeleton, where  $D_R$  and  $D_A$  are the diffusion constants.  $\Delta_T$  is the Laplace operator describing the diffusion-induced concentration changes of the biochemical factors, and its expression will be given in Section 3.1. The saturating Hill functions  $C_{R,e(ij)}^n / (K_R^n + C_{R,e(ij)}^n)$  and  $C_{A,e(ij)}^n / (K_A^n + C_{A,e(ij)}^n)$  in the second items describe the activation in the chemical reactions among RhoA-GTP, GEF, and actomyosin, where  $K_R$  and  $K_A$  are the apparent dissociation constants,  $n$  is the Hill coefficient,  $k_R^{\text{on}}$  and  $k_A^{\text{on}}$  are the self-activation coefficients. The third items describe the self-deactivation, with  $k_R^{\text{off}}$  and  $k_A^{\text{off}}$  being the self-deactivation coefficients. The last item in Eq. (14) defines the mechanical feedback to RhoA activation, where  $k_m^{\text{off}}$  is the mechanical deactivation coefficient. The mechanical feedback factor,  $f(\lambda_{e(ij)})$ , is assumed to be a function of the stretch ratio  $\lambda_{e(ij)} = l_{e(ij)} / l_{n,e(ij)}$  as the Sigmoid function:

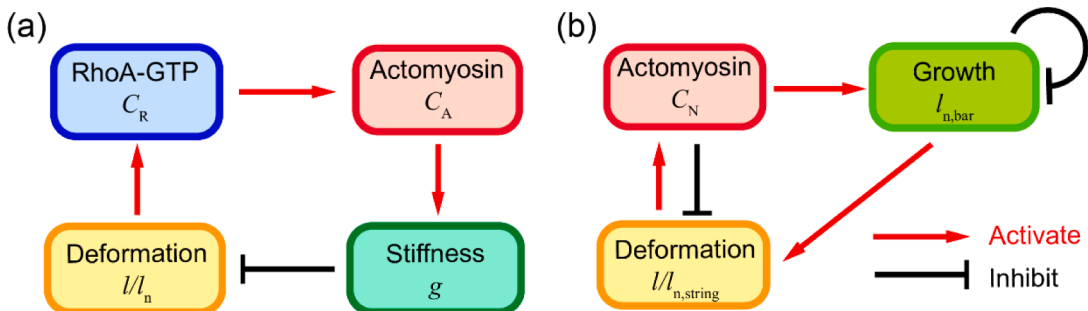


**Fig. 3.** Schematics of the biochemomechanical coupling regulations. (a) The negative feedback loop of active contraction in strings. (b) The regulation loop of growth in bars.

$$f(\lambda_{e(ij)}) = \frac{2}{1 + \exp[k_m(\lambda_{e(ij)} - 1)]}, \quad (16)$$

where  $k_m$  is the sensitivity of mechanical feedback. The Sigmoid function of the stretch ratio ensures the mechanical feedback in an appropriate regime (Yin et al., 2021, 2022). Eq. (16) shows that with the elongation of the element, its mechanical feedback will become weaker, indicating an increase in the concentration of RhoA-GTP.

In the initial state, the tensegrity is prestressed due to the presence of pre-existing residual stresses and active stresses. Then we integrate the effect of actomyosin concentration on the active contraction by considering the chemical feedback to the axial stiffnesses of strings. For brevity, we assume that the reaction and diffusion of biochemical factors occur only in the string elements. The biochemically regulated axial stiffness of the string  $e(ij)$  is given by

$$g_{e(ij)} = g_{0,e(ij)} \exp[k_c(C_{A,e(ij)} - C_A^*)], \quad (17)$$

where  $g_{0,e(ij)}$  is the initial axial stiffness of element  $e(ij)$ ,  $k_c$  is the sensitivity of chemical feedback, and  $C_A^*$  is the stationary actomyosin concentration. The exponential function represents the concentration-dependent modification of the axial stiffness (Miller et al., 2018). According to Eq. (11), the increase in the actomyosin concentration will lead to a larger axial stiffness and a bigger internal force and thus inhibit the elongation of string elements. In turn, the element deformation will be fed back to the RhoA-GTP concentration, which completes the whole regulation loop.

### 2.2.2. Growth of bars

In the dynamic behavior of a cell, its shape may change with the assembly and disassembly of stiffened actin bundles and microtubules, which are integrated by the growth of bars. When F-actins are anchored on the substrate, their directional assembly and disassembly may also result in actin migration, which contributes to the protrusion, polarization, and migration of the cell (Huber et al., 2018; Inagaki and Katsuno, 2017). It has been proved that the protrusion of a polar cell body is independent of the active contraction of the cell cortex but driven by a distinct mechanism (Bischof et al., 2017). Therefore, we introduce another regulation loop to represent the regulation mechanism for the growth of bars, as shown in Fig. 3 (b). The growth of a bar element is regulated by the actomyosin concentrations at both ends,

$$\frac{dl_{n,e(ij)}}{dt} = k_G(C_{N,i} + C_{N,j} - 2C_A^*) \left(2 - \frac{l_{n,e(ij)}}{l_{0,e(ij)}}\right) \frac{l_{n,e(ij)}}{l_{0,e(ij)}}, \quad (18)$$

where  $l_{0,e(ij)}$  is the initial natural length of element  $e(ij)$ ,  $k_G$  is the growth coefficient, and  $C_{N,i}$  is the concentration at node  $i$ , which is given by

$$C_{N,i} = \sum_j C_{A,e(ij)}. \quad (19)$$

The stationary actomyosin concentration  $C_A^*$  defines a threshold of growth, above which the element elongates (polymerizes), and below which the element shrinks (depolymerizes). The linear growth function of node concentrations is here assumed, and the element lengths are limited to ensure their growth in an appropriate regime. Through the mechanical equilibrium and kinematic relation, the growing bars stretch the strings, which represents positive feedback on the concentration of actomyosin and further promotes the growth of bars. This positive feedback mechanism makes it easier for cells to form protrusions. Then, the limit of the element length and the negative feedback loop of active contraction in strings will inhibit the over-growth of the protrusion and lead to a stable cell shape.

### 2.2.3. Cell-substrate interactions

The adhesion between a cell and the extracellular environment has a significant influence on its cytoskeleton dynamics. When a cell adheres to the ECM, the formation of focal adhesions enables the physical and chemical communications between the intracellular cytoskeleton and the ECM (Sun et al., 2022). Coordinated by biochemomechanical coupling processes, focal adhesions have a higher concentration around the periphery of the cell (Deshpande et al., 2008). Neglecting the detailed formation and distribution evolution of focal adhesions, we examine the cell–substrate interaction by the changing constraints at the nodes. Since forces can induce the disassembly of focal adhesions, an adhesion force threshold is assumed to judge the detachment of nodes. Once node  $i$  has been detached from the substrate, it will not be subjected to external forces. Due to the requirement of overall mechanical equilibrium, the node may retrograde and rebuild adhesion with the substrate at a new position. Thus, the adhesion condition of node  $i$  on a rigid substrate can be expressed by

$$\begin{cases} \frac{dp_i}{dt} = \mathbf{0} & (\text{adhered node } i), \quad \text{when } |\mathbf{f}_T| \leq f_{\max}, \\ \mathbf{f}_i = \mathbf{0} & (\text{detached node } i), \quad \text{when } |\mathbf{f}_T| > f_{\max}, \end{cases} \quad (20)$$

where  $\mathbf{p}_i$  is the coordinate vector of node  $i$ ,  $\mathbf{f}_T = -\mathbf{f}_i$  is the traction force applied on the substrate, and  $f_{\max}$  is the threshold of the adhesion force. Besides, it is worth mentioning that the geometric and mechanical properties of the substrate have impacts on the

spreading and movement of cells (Friedl and Gilmour, 2009; Janmey and McCulloch, 2007), but they are omitted here for simplicity.

### 2.3. Summary of the theory

In the above subsections, we have formulated the biochemomechanical coupling tensegrity model of cytoskeletons via a set of fully coupled governing differential equations that integrate the mechanical and chemical fields with biological mechanisms. The governing equations include the mechanical equilibrium condition in Eq. (2) or (4), the kinematic relation in Eq. (6) or (8), the constitutive relation in Eq. (13), the biochemical reactions in Eqs. (14) and (15), and the growth evolution in Eq. (18). Besides, the evolutionary cell–substrate adhesion in Eq. (20) serves as the boundary conditions. These equations will be solved via a numerical scheme, which will be described in the following section. This theory provides a general framework to model the dynamic behaviors of cells under various mechanical, chemical, and biological conditions, as demonstrated in Section 5.

## 3. Numerical scheme

### 3.1. Diffusion of biochemical factors

In our model, the diffusion of biochemical factors in cytoskeletons is converted into mass transfer among the elements in the tensegrity. Chemical diffusion occurs in each pair of connected string elements through the nodes. Take RhoA-GTP as an example. Neglecting the concentration gradient of RhoA-GTP in each element, its diffusion rate is determined by the concentration difference between elements  $e(ij)$  and  $e(ik)$  and the network distance of their centers via the relation,

$$J_R = 2D_R \frac{C_{R,e(ij)} - C_{R,e(ik)}}{l_{n,e(ij)} + l_{n,e(ik)}}, \quad (21)$$

where  $J_R$  is the diffusion flux, and the network distance between adjacent elements is represented by their average length. Considering the condition of mass conservation, the concentration change of RhoA-GTP in  $e(ij)$  induced by the diffusion from  $e(ik)$  is given by

$$\frac{d\hat{C}_R}{dt} = -\frac{J_R}{l_{n,e(ij)}} = 2D_R \frac{C_{R,e(ik)} - C_{R,e(ij)}}{(l_{n,e(ik)} + l_{n,e(ij)})l_{n,e(ij)}}. \quad (22)$$

Assume that the element  $e(ij)$  is connected with  $K_i$  and  $K_j$  string elements at the nodes  $i$  and  $j$ , respectively. Thus, the total diffusion rate is written as

$$D_R \Delta_T C_{R,e(ij)} = \frac{D_R}{l_{n,e(ij)}} \left[ 2 \sum_{K_i} \left( \frac{C_{R,e(iK_i)} - C_{R,e(ij)}}{l_{n,e(iK_i)} + l_{n,e(ij)}} \right) + 2 \sum_{K_j} \left( \frac{C_{R,e(jK_j)} - C_{R,e(ij)}}{l_{n,e(jK_j)} + l_{n,e(ij)}} \right) \right], \quad (23)$$

which the Laplace operator  $\Delta_T$  reflects the diffusion from all neighbor elements, as defined in Eqs. (14) and (15). Eqs. (21) and (23) are reduced forms of Fick's first and second laws, respectively. By this definition, the diffusion between the element and all neighboring elements at both ends is introduced, and the biochemical factors in strings may diffuse into several sub-elements. In the special case when all string elements have the same natural length, Eq. (23) reduces to

$$D_R \Delta_T C_{R,e(ij)} = \frac{D_R}{l_n^2} \left[ \sum_{K_i} (C_{R,e(iK_i)} - C_{R,e(ij)}) + \sum_{K_j} (C_{R,e(jK_j)} - C_{R,e(ij)}) \right]. \quad (24)$$

### 3.2. Mechanical deformation

#### 3.2.1. Structural stiffness matrix method

Since the speed of mechanical responses is in general much faster than that of chemical diffusion, we assume that the deformation of cytoskeleton is quasi-static. Thus the solutions of chemical and mechanical fields can be decoupled.

In this work, the structural stiffness matrix method is extended to numerically solve the incremental deformations of the tensegrity structure from time  $t_k$  to  $t_{k+1} = t_k + \delta t_k$ , with  $\delta t_k$  being an infinitesimal step of time. In this method, we utilize the stiffness matrix and total potential energy of the structure to direct the convergence of the structural configuration toward the self-equilibrated and stable state (Zhang et al., 2013).

Under a given chemical field, the geometric sizes of the tensegrity vary with the externally applied loads. The coordinates of all nodes can be determined from the equilibrium condition in Eq. (2). Then the nodal coordinate matrix  $\mathbf{p}$  is correlated with the external force matrix  $\mathbf{f}$  by (Guest, 2010)

$$\mathbf{K} \cdot d\mathbf{p} = d\mathbf{f}, \quad (25)$$

where  $\mathbf{K}$  denotes the structural stiffness matrix. It is calculated by (Zhang et al., 2013)

$$\mathbf{K} = \frac{d\mathbf{f}(\mathbf{p})}{d\mathbf{p}} = \frac{d\mathbf{f}(\mathbf{p}, \mathbf{t}(\mathbf{p}), \mathbf{l}^{-1}(\mathbf{p}))}{d\mathbf{p}} = \frac{\partial \mathbf{f}}{\partial \mathbf{p}} + \frac{\partial \mathbf{f}}{\partial \mathbf{t}} \cdot \frac{\partial \mathbf{t}}{\partial \mathbf{p}} + \frac{\partial \mathbf{f}}{\partial \mathbf{l}^{-1}} \cdot \frac{\partial \mathbf{l}^{-1}}{\partial \mathbf{p}}, \quad (26)$$

where  $\mathbf{l}^{-1} = [\dots, l_{e(ij)}^{-1}, \dots]^T \in \mathbb{R}^{n_e}$ . Utilizing the equilibrium, kinematic, and constitutive equations, Eq. (26) becomes

$$\mathbf{K} = \mathbf{S} + \mathbf{A} \cdot \mathbf{G} \cdot \mathbf{A}^T - \mathbf{A} \cdot \mathbf{Q} \cdot \mathbf{A}^T, \quad (27)$$

which provides a simple approach to derive the structural stiffness of tensegrity.

For a tensegrity with specified displacement or force boundary conditions, the components of  $\delta\mathbf{p}$  and  $\delta\mathbf{f}$  can be divided into two groups: (i)  $\delta\bar{\mathbf{p}}$  and  $\delta\bar{\mathbf{f}}$ , which are already known, and (ii)  $\delta\tilde{\mathbf{p}}$  and  $\delta\tilde{\mathbf{f}}$ , which are unknown and need to be determined. Thus, the incremental force matrix in Eq. (25) can be partitioned into

$$\begin{bmatrix} \bar{\mathbf{K}} & \tilde{\mathbf{K}} \\ \tilde{\mathbf{K}}^T & \bar{\mathbf{K}} \end{bmatrix} \cdot \begin{bmatrix} \delta\bar{\mathbf{p}} \\ \delta\tilde{\mathbf{p}} \end{bmatrix} = \begin{bmatrix} \delta\tilde{\mathbf{f}} \\ \delta\bar{\mathbf{f}} \end{bmatrix}, \quad (28)$$

where the structural stiffness matrix  $\mathbf{K}$  has been partitioned into four submatrices. The unknown components  $\delta\tilde{\mathbf{p}}$  and  $\delta\tilde{\mathbf{f}}$  can be obtained by

$$\delta\tilde{\mathbf{p}} = \tilde{\mathbf{K}}^{-1} \cdot (\delta\bar{\mathbf{f}} - \tilde{\mathbf{K}}^T \cdot \delta\bar{\mathbf{p}}), \quad (29)$$

$$\delta\tilde{\mathbf{f}} = \bar{\mathbf{K}} \cdot \delta\bar{\mathbf{p}} + \tilde{\mathbf{K}} \cdot \delta\tilde{\mathbf{p}}. \quad (30)$$

In the simulations, the Newton–Raphson iteration method is utilized to eliminate the out-of-balance forces, which guarantees both the precision and the convergence speed. The nodal coordinate  $\mathbf{p}_{k+1}$  and the external force  $\mathbf{f}_{k+1}$  at time  $t_{k+1}$  are determined via the following steps.

- (1) Define the nodal coordinate matrix  $\mathbf{p}_k$  at time  $t_k$  as the initial positions  $\mathbf{p}_{(k+1,0)}$ , determine the increments of forces  $\delta\bar{\mathbf{f}}_k$  and displacements  $\delta\bar{\mathbf{p}}_k$  from the boundary conditions, and then initialize the external force  $\bar{\mathbf{f}}_{k+1} = \bar{\mathbf{f}}_k + \delta\bar{\mathbf{f}}_k$  and  $\tilde{\mathbf{f}}_{k+1} = \mathbf{0}$ .
- (2) Calculate the structural stiffness matrix  $\mathbf{K}_{(k+1,0)}$  from  $\mathbf{p}_{(k+1,0)}$ , and solve the submatrices  $\bar{\mathbf{K}}_{(k+1,0)}$ ,  $\tilde{\mathbf{K}}_{(k+1,0)}$ , and  $\tilde{\mathbf{K}}_{(k+1,0)}$ . Then the unknown increment  $\delta\tilde{\mathbf{p}}_{(k+1,0)}$  can be determined by

$$\delta\tilde{\mathbf{p}}_{(k+1,0)} = \tilde{\mathbf{K}}_{(k+1,0)}^{-1} \cdot (\delta\bar{\mathbf{f}}_k - \tilde{\mathbf{K}}_{(k+1,0)}^T \cdot \delta\bar{\mathbf{p}}_k). \quad (31)$$

Give the increment  $\delta\mathbf{p}_{(k+1,0)}$  by

$$\delta\mathbf{p}_{(k+1,0)} = \begin{bmatrix} \delta\bar{\mathbf{p}}_k \\ \delta\tilde{\mathbf{p}}_{(k+1,0)} \end{bmatrix}. \quad (32)$$

- (3) Calculate the nodal coordinates at the first step by  $\mathbf{p}_{(k+1,1)} = \mathbf{p}_{(k+1,0)} + \delta\mathbf{p}_{(k+1,0)}$ , and update the equilibrium matrix  $\mathbf{A}_{(k+1,1)}$  and the internal force  $\mathbf{t}_{(k+1,1)}$ . Determine the out-of-balance force  $\mathbf{R}_{(k+1,1)}$  by

$$\mathbf{R}_{(k+1,1)} = \mathbf{f}_{k+1} - \mathbf{A}_{(k+1,1)} \cdot \mathbf{t}_{(k+1,1)}. \quad (33)$$

The component  $\tilde{R}_i$  on the force boundary is used to judge the equilibrium by

$$\max_i |\tilde{R}_i| < R_{\max}, \quad (34)$$

where  $R_{\max}$  is the force tolerance of equilibrium. Set the number of the iterative step  $m=1$ . If Eq. (34) is satisfied, go to Step (6); otherwise, enter the iteration in Step (4).

- (4) At the  $m$ th iterative step, calculate the structural stiffness matrix  $\mathbf{K}_{(k+1,m)}$  from  $\mathbf{p}_{(k+1,m)}$ , and the coordinate increments  $\delta\mathbf{p}_{(k+1,m)}$  by

$$\delta\mathbf{p}_{(k+1,m)} = \mathbf{K}_{(k+1,m)}^{-1} \cdot \mathbf{R}_{(k+1,m)}. \quad (35)$$

Then solve the nodal coordinate  $\mathbf{p}_{(k+1,m+1)}$  and the out-of-balance force  $\mathbf{R}_{(k+1,m+1)}$  by

$$\mathbf{p}_{(k+1,m+1)} = \mathbf{p}_{(k+1,m)} + \delta\mathbf{p}_{(k+1,m)}, \quad (36)$$

$$\mathbf{R}_{(k+1,m+1)} = \mathbf{f}_{k+1} - \mathbf{A}_{(k+1,m+1)} \cdot \mathbf{t}_{(k+1,m+1)}. \quad (37)$$

(5) If Eq. (34) is satisfied, go to Step (6); otherwise, set  $m=m+1$  and go to Step (4).

(6) The structure reaches the mechanical equilibrium at  $\mathbf{p}_{(k+1,m)}$ . Update the nodal coordinate matrix  $\mathbf{p}_{k+1}$  and the external force matrix  $\mathbf{f}_{k+1}$  by

$$\mathbf{p}_{k+1} = \mathbf{p}_{(k+1,m)}, \quad \mathbf{f}_{k+1} = \begin{bmatrix} \bar{\mathbf{f}}_k + \delta\bar{\mathbf{f}}_k \\ \mathbf{R}_{(k+1,m)} \end{bmatrix}. \quad (38)$$

### 3.2.2. Time discretization

The initial self-equilibrated configuration of the cytoskeleton tensegrity needs to be obtained via a form-finding process. To this end, the numerical method for the quasi-static deformation analysis in Section 3.2.1 is used with the known external force  $\delta\bar{\mathbf{f}} = \mathbf{0}$ . The structural stiffness matrix  $\mathbf{K}$  guides the calculation to rapidly converge to a self-equilibrated and stable configuration (Zhang et al., 2014b; Zhang et al., 2013). During the incremental step from  $t_k$  to  $t_{k+1}$ , we take a semi-implicit modified Euler method to integrate the biochemical fields, including the concentrations in the strings, the growth of bars, and the cell–substrate adhesion forces. Specifically, for each biochemical variable  $C$ , we first give a prediction  $\hat{C}_{k+1}$  based on the original values ( $C_k$ ,  $l_k$ , ...) at time  $t_k$  by

$$\hat{C}_{k+1} = C_k + \dot{C}(C_k, l_k, \dots) \delta t_k, \quad (39)$$

where the evolution function  $\dot{C}(C, l, \dots)$  is defined by Eqs. (14) and (15). Then, based on the value of  $\hat{C}_{k+1}$  in Eq. (39), the prediction of mechanical equilibrium  $\hat{l}_{k+1}$  is solved from the structural stiffness matrix method in Section 3.2.1. The updated value  $C_{k+1}$  at time  $t_{k+1}$  is given by

$$C_{k+1} = C_k + \frac{1}{2} \delta t_k [\dot{C}(C_k, l_k, \dots) + \dot{C}(\hat{C}_{k+1}, \hat{l}_{k+1}, \dots)]. \quad (40)$$

Finally, the structural stiffness matrix method is applied to calculate the nodal coordinate matrix  $\mathbf{p}_{k+1}$  at time  $t_{k+1}$  from the updated biochemical field  $C_{k+1}$ .

Repeating the above time-stepping procedure, the evolutions of all biochemical and mechanical quantities with time  $t$  can be simulated.

### 3.3. Dynamic responses

In the above subsections, we have assumed that the deformation of the tensegrity is quasi-static and thus the chemical and mechanical fields can be decoupled in the solution. In some processes, however, the timescales of mechanical responses and chemical reaction–diffusion are comparable. In this case, the dynamic effects should be considered and the numerical scheme is modified as follows to simulate the evolutions in the mechanical and chemical fields.

As in the finite element method, we divide the mass of each element at its both nodes. Thus, the consistent mass matrix  $\mathbf{M} \in \mathbb{R}^{n_n \times n_n}$  is expressed as

$$\mathbf{M} = \frac{1}{4} \text{abs}(\mathbf{C})^T \cdot \mathbf{m} \cdot \text{abs}(\mathbf{C}) + \frac{1}{12} \mathbf{C}^T \cdot \mathbf{m} \cdot \mathbf{C}, \quad (41)$$

where the components in the matrix  $\text{abs}(\mathbf{C})$  equal to the absolute values of those in the connection matrix  $\mathbf{C}$ , and  $\mathbf{m} = \text{diag}(\dots, m_{e(ij)}, \dots) \in \mathbb{R}^{n_e \times n_e}$  is a diagonal matrix constructed by the masses of all elements. Then, the kinematic equation is expressed as

$$\widehat{\mathbf{M}} \cdot \mathbf{a} = \mathbf{f} - \mathbf{A} \cdot \mathbf{t}, \quad (42)$$

where the mass matrix  $\widehat{\mathbf{M}} \in \mathbb{R}^{3n_n \times 3n_n}$  is the second-order formulation of the Kronecker product  $\mathbf{M} \otimes \mathbf{I}$ , and the nodal acceleration vector  $\mathbf{a} = [\dots, (d^2\mathbf{p}_i/dt^2)^T, \dots]^T \in \mathbb{R}^{3n_n}$  contains the acceleration components at all nodes. Thus, the dynamic deformation of the tensegrity is determined from the motion of the nodal coordinate vector  $\mathbf{p}$  by

$$\frac{d\mathbf{p}}{dt} = \mathbf{v}, \quad (43)$$

$$\frac{d\mathbf{v}}{dt} = \mathbf{a} = \widehat{\mathbf{M}}^{-1} \cdot (\mathbf{f} - \mathbf{A} \cdot \mathbf{t}), \quad (44)$$

where the nodal velocity vector  $\mathbf{v} = [\dots, (\mathbf{d}\mathbf{p}_i/dt)^T, \dots]^T \in \mathbb{R}^{3n_0}$  contains the velocity components at all nodes.

At the incremental step from  $t_k$  to  $t_{k+1}$ , the evolutions of biochemical variables in Eqs. (14) and (15) and the nodal coordinate in Eqs. (43) and (44) are discretized following the same scheme in Section 3.2.2. Both the biochemical and mechanical variables can be solved from the modified Euler method. Repeating the time-stepping procedure, the dynamic responses under specified external forces and biochemical fields are obtained explicitly.

### 3.4. Verification examples

We consider the pure chemical diffusion process in a single direction to examine the numerical implementation method in the discrete tensegrity. To clearly show this, only one biochemical variable is considered here, and all of its activations and deactivations are neglected. The deformation of the fiber is completely constrained, and the zero-flux conditions are set by connecting no other element with the nodes at both ends. The initial distribution of concentration is set as

$$\begin{cases} C = 1, & x \in [0, 10 \mu\text{m}], \\ C = 0, & x \in (10 \mu\text{m}, 50 \mu\text{m}], \end{cases} \quad (45)$$

where  $x$  is the coordinate.

Fig. 4(a) shows the spatiotemporal evolution of the concentration, in which the fiber is divided into 5 elements in the simulation. Even if a rough division method is adopted, the simulation result can still reproduce the same spatiotemporal evolution as the theoretical solution (Fig. 4(b)). It can be seen in Fig. 4(c) that simulation results under different element divisions (including elements with a uniform length distribution and elements with a random length distribution) all agree quantitatively with the theoretical solution. This suggests that our model shows high robustness to the element division in describing the diffusion process.

## 4. Biochemomechanical stability analysis

Before the investigation of the active deformation and motion of a multiscale cytoskeleton, we first reveal the dynamic behaviors of

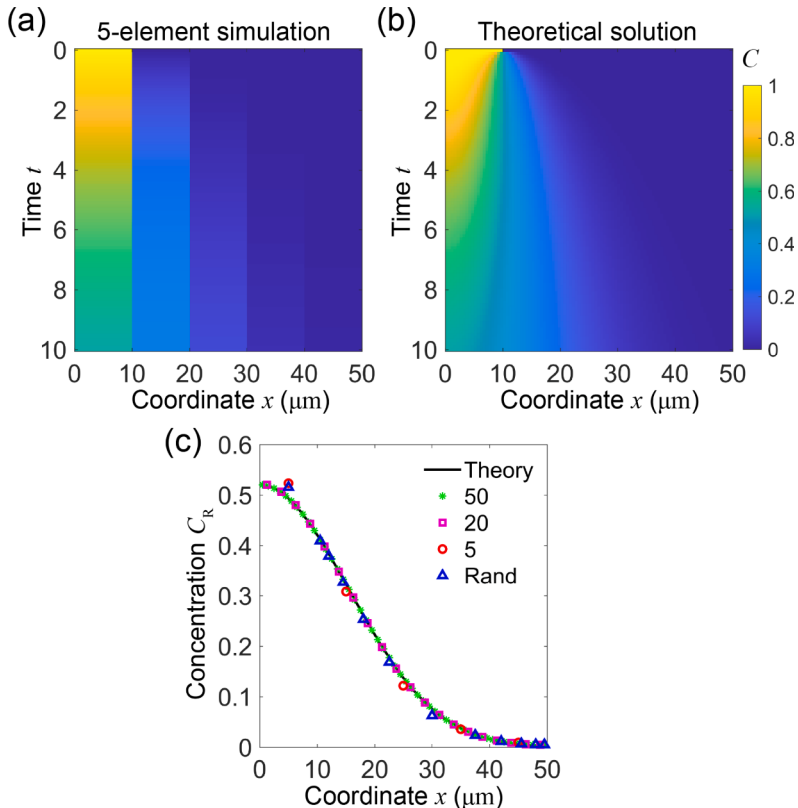


**Fig. 4.** Numerical simulations of the diffusion on a fiber. (a) The simulation of the concentration spatiotemporal evolution, in which the fiber is divided into 5 string elements. The concentration at coordinate  $x$  is given by the concentration of the element there. (b) The theoretical solution of the concentration spatiotemporal evolution. (c) The comparison between the concentration distributions of the theory and different simulations (50, 20, and 5 elements with uniform length, and elements with random length) at time  $t = 10$ . Time  $t$  is normalized by a characteristic time  $t_c = 10 / 3\text{s}$ .

a single element (either a string or a bar) in the tensegrity model that is dominated by the biochemomechanical coupling mechanisms. In this section, for illustration, we will perform the linear stability analysis of a string. The dynamic behavior of bars can be analyzed analogously but is omitted here.

#### 4.1. Multiscale model of an actomyosin string

The string represents a piece of cell cortex with a dense actomyosin network. Fig. 5 shows its multiscale structure, which comprises F-actins connected by myosin protein monomers or filaments of myosin. The activity of myosin motors and the microscopic structure of cross-linked F-actins are mediated by the mechanical forces via the biochemomechanical signaling pathway. Due to the biochemomechanical coupling regulation, the deformations and chemical fields in the string may evolve with time into diverse dynamic states. In this section, we first derive the analytical solution of the stationary state of a string, and then study its dynamic states under the biochemomechanical feedback regulation through a linear stability analysis.

#### 4.2. Stationary state analysis

In the stationary biochemomechanical state of the string, its deformation and concentration fields are in equilibrium. We ignore the spatial difference of these fields within a single element, and thus the string degenerates into a nonlinear dynamic system without spatial gradient. Introduce the characteristic length  $l_c$ , the characteristic time  $t_c = l_c^2 / D_R$  and the characteristic force  $f_c$  in a string. Then all other parameters and variables are normalized by these parameters. In the following analysis, we apply a pair of constant forces  $t^*$  on both ends of the string to examine the effect of prestresses, as shown in Fig. 5. Let  $l^*$ ,  $\lambda^*$ ,  $C_R^*$ , and  $C_A^*$  denote the normalized stationary length, stationary stretch ratio, RhoA-GTP concentration, and actomyosin concentration, respectively. The fixed point (or stationary state)  $(l^*, C_R^*, C_A^*)$  satisfies both the constitutive relation in Eq. (13) and the zero biochemical evolutions in Eqs. (14) and (15), which can be rewritten respectively as

$$g_0(l^* - l_n) = t^*, \quad (46)$$

$$k_R^{on} \frac{C_R^{*n}}{K_R^n + C_R^{*n}} (1 - C_R^*) - k_R^{off} C_R^* - k_m^{off} f(\lambda^*) C_R^* = 0, \quad (47)$$

$$k_A^{on} \frac{C_A^{*n}}{K_A^n + C_A^{*n}} (1 - C_A^*) - k_A^{off} C_A^* = 0. \quad (48)$$

The normalized parameters and representative values adopted in our analysis and simulations are listed in Table 1.

Eq. (46) shows that the stationary constitutive relation assumed for the mechanical deformation of the string is linear. In what follows, we will investigate the dependence of the stationary chemical fields on the model parameters. The stationary RhoA-GTP concentration  $C_R^*$  is implicitly related to the self-activation and deactivation, and the mechanical feedback as well. As shown in Fig. 6(a), the stationary RhoA-GTP concentration  $C_R^*$  is dictated by the rival relationship between the coefficients of self-activation and deactivation,  $k_R^{on}$  and  $k_R^{off}$ . With increasing self-activation  $k_R^{on}$  (white arrow), the stationary RhoA-GTP concentration  $C_R^*$  decreases nonlinearly but monotonously in the given scope, which indicates the mapping relation between  $C_R^*$  and  $k_R^{on}$ . The influences of mechanical feedback on  $C_R^*$  are shown in Fig. 6(b). The self-activation  $k_R^{on}$  (white arrow) is amplified with the increase in the mechanical

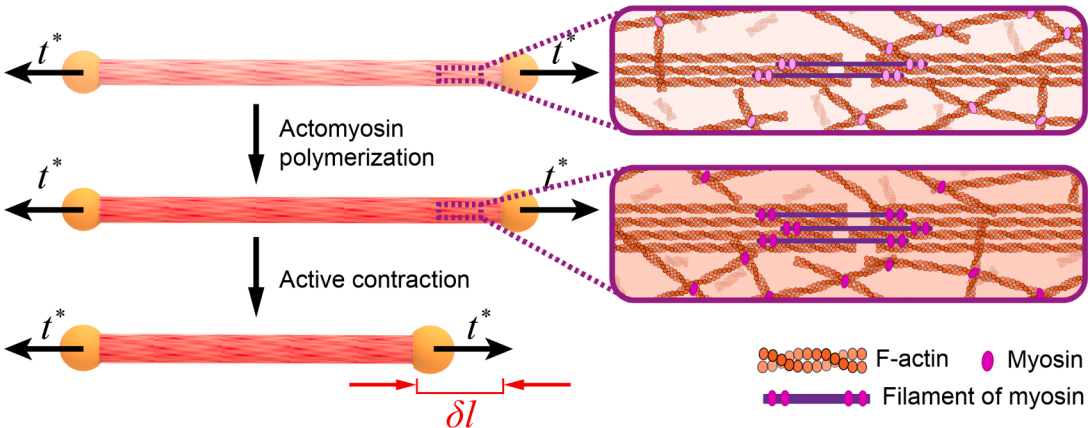


**Fig. 5.** Multiscale model of an active biochemomechanical string. The mechanical forces mediate the activity of myosin motors and the microscopic structure of cross-linked F-actins via the biochemomechanical signaling module. Higher-order cytoskeletal stress fibers form to generate active forces. When the string is stretched, its deformation up-regulates the activation of RhoA-GTP, which induces the actomyosin polymerization and thus leads to a denser network and stronger myosin activity. The microstructural change causes the macroscopic active contraction of the string, which, in turn, prevents its further elongation.

**Table 1**

Parameters used in the analysis and simulations.

Parameters	Values	References
Diffusivity of RhoA-GTP, $D_R$	$0.3 \mu\text{m}^2 \cdot \text{s}^{-1}$	Bement et al. (2015)
Diffusivity of actomyosin, $D_A$	$0.3 \mu\text{m}^2 \cdot \text{s}^{-1}$	Dawes and Munro (2011)
Characteristic length, $l_c$	$1 \mu\text{m}$	Assumed
Characteristic force, $f_c$	$1 \text{nN}$	Assumed
Apparent dissociation constant of RhoA-GTP, $K_R$	0.5	Ferrell et al. (2011)
Apparent dissociation constant of actomyosin, $K_A$	0.5	Ferrell et al. (2011)
Self-activation coefficient of actomyosin, $k_A^{\text{on}}$	3	Lin et al. (2018)
Self-deactivation coefficient of actomyosin, $k_A^{\text{off}}$	1	Bement et al. (2015)
Self-deactivation coefficient of RhoA-GTP, $k_R^{\text{off}}$	0	Bement et al. (2015)
Mechanical deactivation coefficient of RhoA-GTP, $k_m^{\text{off}}$	2	Yin et al. (2021)
Sensitivity of mechanical feedback, $k_m$	10	Assumed
Hill coefficient, $n$	8	Ferrell et al. (2011)
Sensitivity of chemical feedback, $k_c$	8	Assumed
Stationary string stiffness, $g_0 \cdot \text{String}$	10	Lin et al. (2018)
Bar stiffness, $g_0 \cdot \text{Bar}$	50	Assumed
Stationary RhoA-GTP concentration, $C_R^*$	0.5	Assumed
Internal force, $t^*$	2	Hannezo et al. (2014)
Natural length, $l_n$	1	Assumed

deactivation coefficient  $k_m^{\text{off}}$  and the decrease in the internal force  $t^*$ . This implies the mechanical cues influence the RhoA-GTP deactivation process and represent positive feedback on the concentration of RhoA-GTP.

In addition, the stationary state of the chemical field  $C_A^*$  can be explicitly determined under a fixed value of  $C_R^*$ . Fig. 6(c) shows how self-activation and deactivation of actomyosin regulate the stationary actomyosin  $C_A^*$ , which reflects the effects of pure chemical reactions. The concentration  $C_A^*$  increases with the self-activation and decreases with the deactivation. The effect of chemical reactions between RhoA-GTP and actomyosin can be described by the Hill function, as shown in Fig. 6(d). The stationary actomyosin  $C_A^*$  exhibits a high gradient variation across the diagonal. When the stationary RhoA-GTP concentration  $C_R^*$  is lower than the apparent dissociation constant of actomyosin  $K_A$ , the stationary actomyosin  $C_A^*$  will keep a lower value. As  $C_R^*$  exceeds the apparent dissociation constant  $K_A$ ,  $C_A^*$  will increase sharply. Finally, a stationary RhoA-GTP concentration  $C_R^*$  higher than the apparent dissociation constant of actomyosin  $K_A$  will render a higher value of stationary actomyosin  $C_A^*$ .

#### 4.3. Linear stability analysis

We now analyze the dynamic stability of the stationary state through the linear stability analysis. Introducing infinitesimal perturbations ( $\delta l$ ,  $\delta C_R$ ,  $\delta C_A$ ) to the stationary state ( $l^*$ ,  $C_R^*$ ,  $C_A^*$ ), the variables ( $l$ ,  $C_R$ ,  $C_A$ ) are written as

$$(l, C_R, C_A) = \left( l_n + \frac{t^*}{g_0} + \delta l, C_R^* + \delta C_R, C_A^* + \delta C_A \right). \quad (49)$$

Substituting Eq. (49) into the constitutive relation in Eq. (13), the perturbed mechanical equilibrium equation is expressed as

$$t^* = \left( \frac{t^*}{g_0} + \delta l \right) g_0 \exp[k_c(\delta C_A)]. \quad (50)$$

Eq. (50) can be linearized by neglecting the high-order infinitesimals. Then, the relation between the geometric perturbation  $\delta l$  and the chemical perturbation  $\delta C_A$  is obtained as

$$\delta l = -\frac{t^* k_c \delta C_A}{g_0}, \quad (51)$$

where the internal force  $t^*$  is a constant. Integrating the geometric perturbation in Eq. (51) into the chemical evolutions in Eqs. (14) and (15). Neglecting the contribution of diffusion, the incremental chemical evolutions are given as

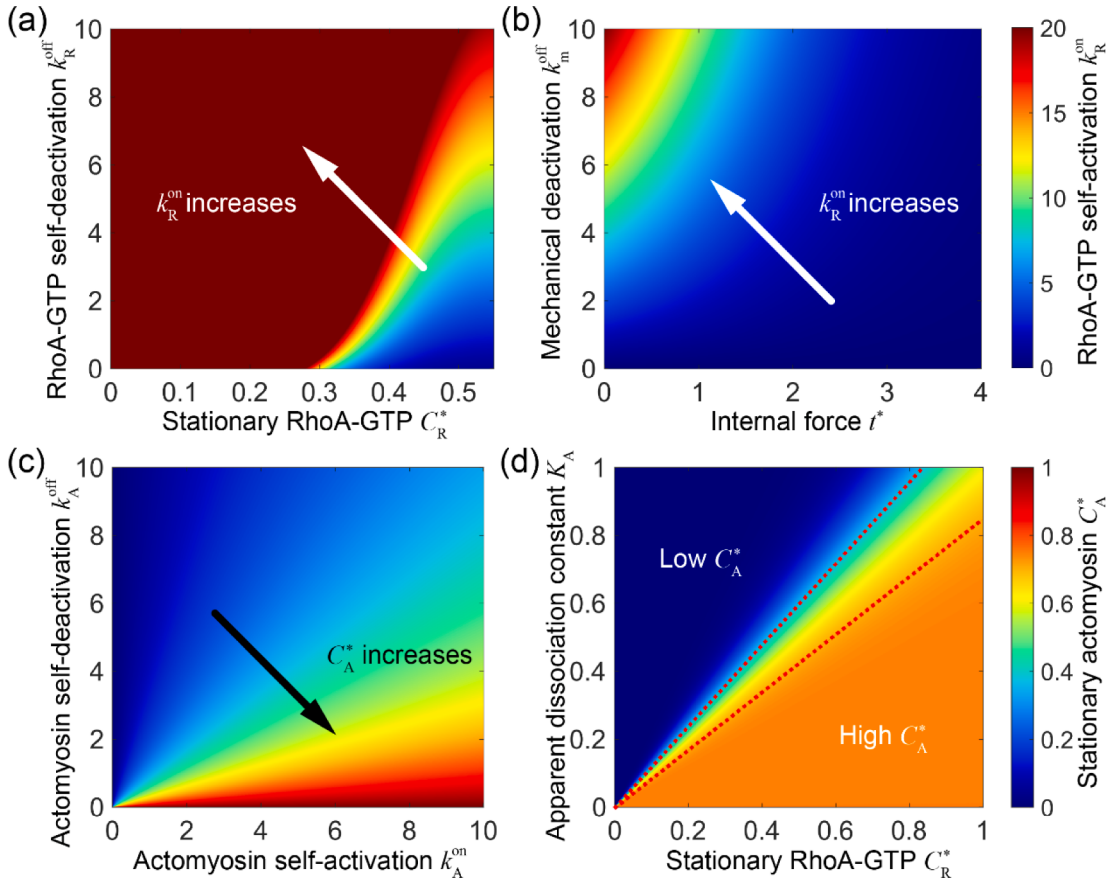


**Fig. 6.** The stationary biochemomechanical state of a string. (a) The mapping relation between coefficients of the RhoA-GTP self-activation and deactivation,  $k_R^{\text{on}}$  and  $k_R^{\text{off}}$ , and the stationary RhoA-GTP  $C_R^*$ . (b) The RhoA-GTP self-activation coefficient  $k_R^{\text{on}}$  regulated by the mechanical feedback parameters. The dependence of the stationary actomyosin  $C_A^*$  on (c) the actomyosin self-activation and deactivation coefficients  $k_A^{\text{on}}$  and  $k_A^{\text{off}}$  and (d) the stationary RhoA-GTP  $C_R^*$  and the apparent dissociation constant  $K_A$ .

$$\frac{d\delta C_R}{dt} = \left\{ k_R^{\text{on}} \frac{n(1 - C_R^*) K_R^n - C_R^*(K_R^n + C_R^{*n}) C_R^{*(n-1)}}{(K_R^n + C_R^{*n})^2} - [k_R^{\text{off}} + k_m^{\text{off}} f(\lambda^*)] \right\} \delta C_R + k_m^{\text{off}} [\partial_{(\lambda^*)} f(\lambda^*)] \frac{C_R^* t^* k_c}{l_n g_0} \delta C_A, \quad (52)$$

$$\frac{d\delta C_A}{dt} = k_A^{\text{on}} \frac{n(1 - C_A^*) K_A^n C_R^{*(n-1)}}{(K_A^n + C_R^{*n})^2} \delta C_R - \left[ k_A^{\text{on}} \frac{C_R^{*n}}{(K_A^n + C_R^{*n})} + k_A^{\text{off}} \right] \delta C_A. \quad (53)$$

The Jacobian matrix  $\mathbf{J}$  of Eqs. (52) and (53) at the fixed point  $(l^*, C_R^*, C_A^*)$  is defined by

$$\begin{bmatrix} \frac{d\delta C_R}{dt} \\ \frac{d\delta C_A}{dt} \end{bmatrix} = \mathbf{J} \cdot \begin{bmatrix} \delta C_R \\ \delta C_A \end{bmatrix} = \begin{bmatrix} J_{11} & J_{12} \\ J_{21} & J_{22} \end{bmatrix} \cdot \begin{bmatrix} \delta C_R \\ \delta C_A \end{bmatrix}, \quad (54)$$

where

$$\begin{aligned}
J_{11} &= k_R^{\text{on}} \frac{n(1 - C_R^*) K_R^n - C_R^*(K_R^n + C_R^{*n})]{C_R^{*(n-1)}}}{(K_R^n + C_R^{*n})^2} \\
&\quad - k_R^{\text{off}} - 2k_m^{\text{off}} \left[ 1 + \exp\left(\frac{t^* k_m}{g_0 l_n}\right) \right]^{-1}, \\
J_{12} &= -2k_m^{\text{off}} k_m \exp\left(\frac{t^* k_m}{g_0 l_n}\right) \left[ 1 + \exp\left(\frac{t^* k_m}{g_0 l_n}\right) \right]^{-2} \frac{C_R^* t^* k_c}{l_n g_0}, \\
J_{21} &= k_A^{\text{on}} \frac{n(1 - C_A^*) K_A^n C_R^{*(n-1)}}{(K_A^n + C_R^{*n})^2}, \\
J_{22} &= -k_A^{\text{on}} \frac{C_R^{*n}}{(K_A^n + C_R^{*n})} - k_A^{\text{off}}.
\end{aligned} \tag{55}$$

The Jacobian matrix  $\mathbf{J}$  has two eigenvalues, which determine the stability of the stationary state ( $t^*$ ,  $C_R^*$ ,  $C_A^*$ ). Only when the real parts of both eigenvalues are negative, is the system stable. Specifically, the characteristic equation of an active biochemomechanical string is written as

$$\zeta^2 - \text{tr}(\mathbf{J})\zeta + \det(\mathbf{J}) = 0, \tag{56}$$

from which the eigenvalue  $\zeta$  can be solved. Depending on the values of  $\text{tr}(\mathbf{J})$  and  $\det(\mathbf{J})$ , the system has the following three possible states.

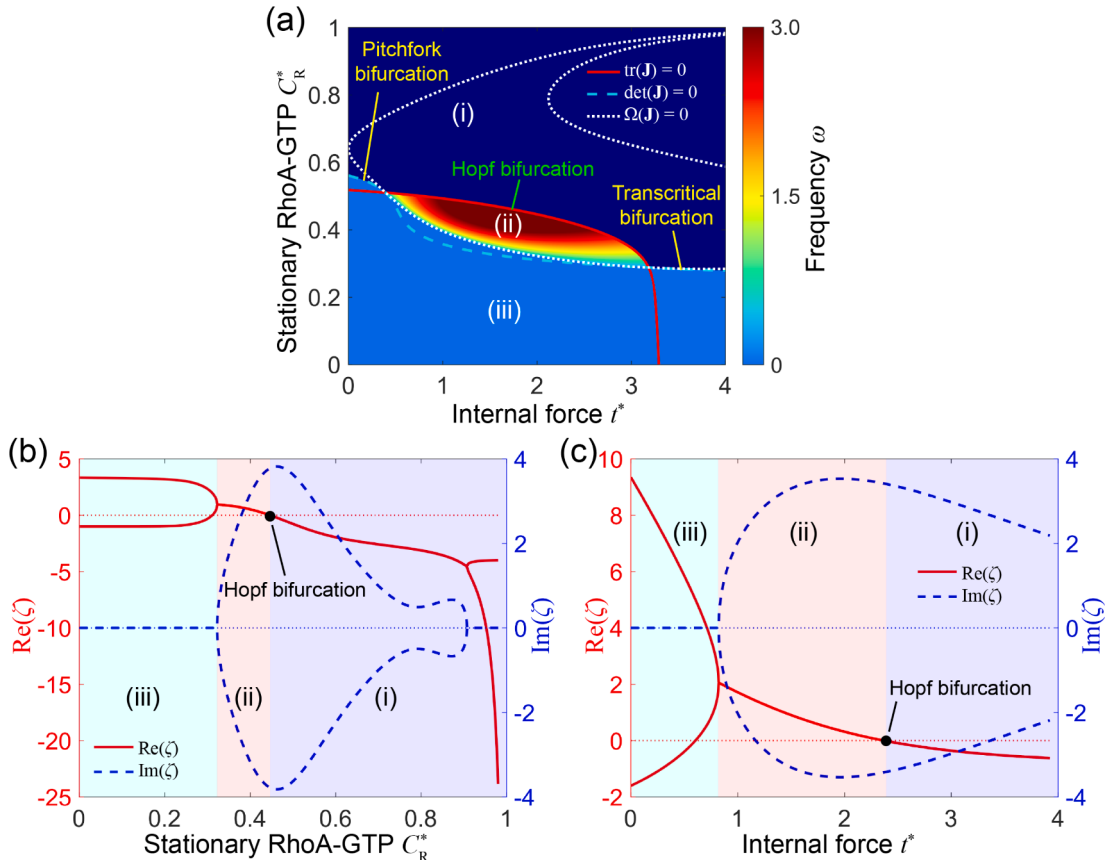


**Fig. 7.** Influences of mechanical and chemical cues on the transitions among the three dynamic states. (a) The phase diagram jointly regulated by the internal force  $t^*$  and the stationary RhoA-GTP  $C_R^*$ . The lines show the positive and negative boundaries of key variables ( $\text{tr}(\mathbf{J})$ ,  $\det(\mathbf{J})$ , and  $\Omega(\mathbf{J})$ ) determining eigenvalues of the Jacobian matrix  $\mathbf{J}$  and the dynamic state. Three regions are distinguished as (i) stable, (ii) oscillatory, and (iii) unstable. Red solid lines between regions (i) and (ii) correspond to Hopf bifurcation, and cyan dash lines between regions (i) and (iii) correspond to pitchfork and transcritical bifurcations. In the oscillatory region, the heat map corresponds to the oscillatory frequency  $\omega$  ( $\text{Im}(\zeta)$ ). (b) The eigenvalue  $\zeta$  versus the stationary RhoA-GTP  $C_R^*$ . Here, the real part  $\text{Re}(\zeta)$  and the imaginary part  $\text{Im}(\zeta)$  are plotted as red solid and blue dashed lines, respectively. The corresponding dynamic states of (i) stable, (ii) oscillatory, and (iii) unstable are distinguished by the background colors. The black point marks Hopf bifurcation. (c) The eigenvalue  $\zeta$  versus the internal force  $t^*$ .

- (i) *Stable State*: If  $\text{tr}(\mathbf{J}) < 0$  and  $\det(\mathbf{J}) > 0$ , then the real parts of both eigenvalues are negative, that is,  $\text{Re}(\zeta) < 0$ , meaning that the stationary state is stable. In this case, the perturbations will settle down to equilibrium. Further, if the stable state satisfies  $\Omega(\mathbf{J}) = \text{tr}^2(\mathbf{J}) - 4\det(\mathbf{J}) < 0$ , then the imaginary parts of the two eigenvalues satisfy  $\text{Im}(\zeta) \neq 0$  and the system will also converge to the stationary state gradually. During this process, the perturbations will decay along a spiral path in the phase plane.
- (ii) *Oscillatory State*: If  $\text{tr}(\mathbf{J}) > 0$  and  $\Omega(\mathbf{J}) < 0$ , then both eigenvalues satisfy  $\text{Re}(\zeta) > 0$  and  $\text{Im}(\zeta) \neq 0$ , meaning that the stationary state is oscillatory. In this situation, the perturbations will grow along a spiral path and finally approach a limit cycle oscillating around the stationary state in the phase plane.
- (iii) *Unstable State*: Otherwise, the eigenvalues are real, and there exists at least an eigenvalue that satisfies  $\zeta > 0$ , meaning that the stationary state is unstable. In this case, the perturbations will collapse to an extreme value or another stationary state.

#### 4.4. Parametric analysis

Based on the above linear stability analysis, we perform a parametric study to capture the dominant features of the active behaviors of an actomyosin string and scrutinize the influences of mechanical and chemical cues on the transitions among the three states. Fig. 7 (a) shows the phase diagram regulated by the internal force  $t^*$  and the stationary RhoA-GTP  $C_R^*$ . The stable state (i) occupies the top of

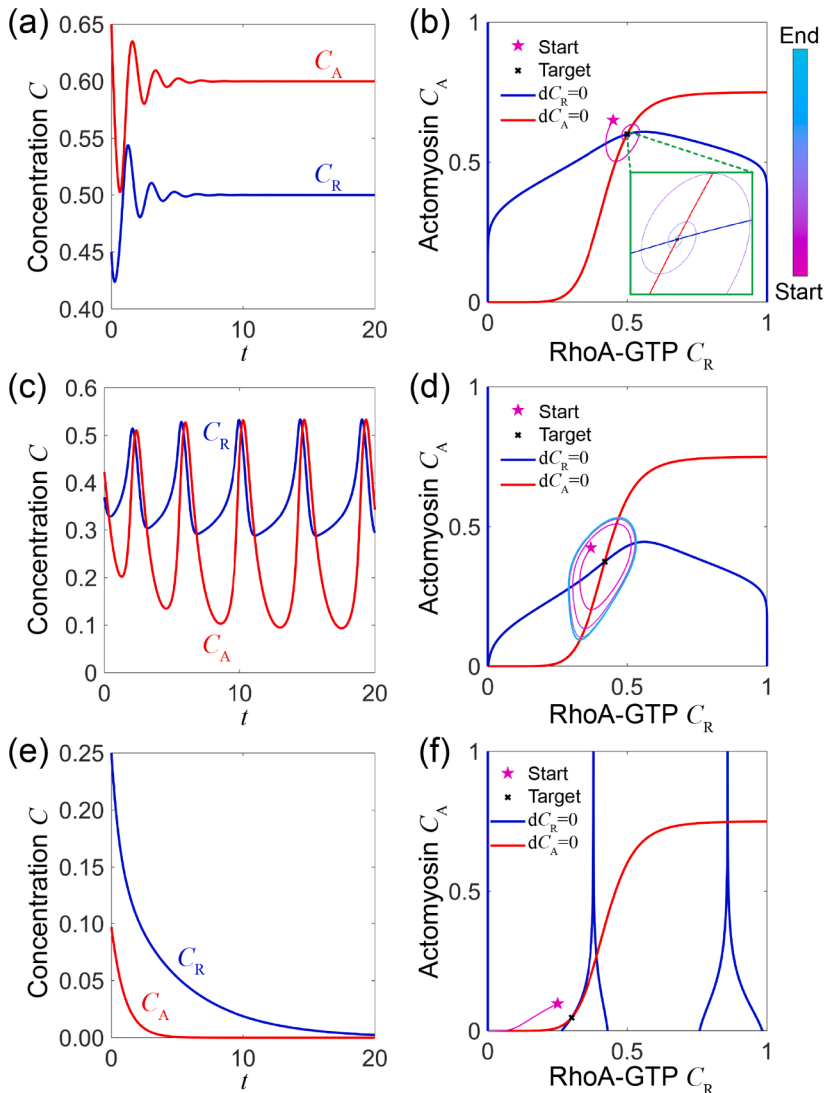


**Fig. 8.** Numerical simulations of an actomyosin string, with  $C_R^* = 0.5$  (a) and (b),  $C_R^* = 0.42$  (c) and (d),  $C_R^* = 0.3$  (e) and (f). The variable evolutions under different parameters are distinguished into three states: (a) stable, (c) oscillatory, and (e) unstable. The phase portraits show the overall pictures of (b) stable, (d) oscillatory, and (f) unstable trajectories in the phase plane of the concentrations of RhoA-GTP  $C_R$  and actomyosin  $C_A$ . Every intersection of nullclines, i.e.,  $dC_R = 0$  and  $dC_A = 0$ , is a fixed point (stationary state). A perturbed position (magenta star) around the target fixed point (black cross) is taken as the start. The colors of the trajectories mark the time from the start to the end.

the phase diagram, suggesting that with a high stationary RhoA-GTP  $C_R^*$ , the chemical reactions of biochemical factors will stabilize the system. The scope of the oscillatory state (ii) can be found only in the middle position (ii) in Fig. 7(a). The heat map in this region shows the frequency of oscillation  $\omega \sim 3t_c^{-1}$ . It is found that the period  $T \sim 2\pi t_c / 3$  is on the order of a few seconds to tens of seconds, which is comparable to experimental observations of a rich variety of cells (Giannone et al., 2004; Salbreux et al., 2007; Sedzinski et al., 2011; Solon et al., 2009). The unstable region (iii) shrinks as the internal force increases, indicating that active contraction forces positively contribute to the stability of structural deformation and chemical reaction.

Next we examine how the transition among the three states, namely bifurcations, occurs with the variation of parameters. For the parameters in region (i), the fixed point is stable, while it will lose its stability when the parameters are beyond this range. At the boundary between (i) and (ii) [i.e., the red solid line in Fig. 7(a)], Hopf bifurcation will occur and lead to the oscillation. At the boundary between (i) and (iii) [i.e., the cyan dash line in Fig. 7(a)], zero-eigenvalue bifurcation (including pitchfork and transcritical bifurcations) will occur and lead to the collapse. Fig. 7(b) and (c) show the variations of the eigenvalues  $\zeta$  with respect to the stationary RhoA-GTP  $C_R^*$  and the internal force  $t^*$ , respectively. The transition among the three states can be induced by the changing either  $C_R^*$  or  $t^*$ . In stable state (i), there exists no eigenvalue that satisfies  $\text{Re}(\zeta) > 0$ , and then the fixed point is stable. The decrease of  $C_R^*$  or  $t^*$  will increase the trace  $\text{tr}(J)$  and thus the real part  $\text{Re}(\zeta)$ . The threshold  $\text{Re}(\zeta) = 0$  represents the onset of Hopf bifurcation. As the imaginary parts of eigenvalues are untrivial, the oscillatory state (ii) will emerge. The further decrease of  $C_R^*$  or  $t^*$  will give rise to the reduction of the oscillatory frequency. Finally, when  $\text{Im}(\zeta) = 0$ , the oscillatory state (ii) will transform into the unstable state (iii).

It is well-known that migrating cells can sense the surrounding mechanical and chemical cues to guide their directional movements in complex ECMs during cancer invasion, embryonic development, and immune response (Lin et al., 2017; Sunyer and Trepot, 2020; Van Haastert and Devreotes, 2004). Myosin-induced cortical actin network contraction plays an essential role in these processes. It not only regulates cellular deformation and morphology for adapting to the narrow pores in the ECMs (Lomakin et al., 2020; Venturini et al., 2020) but also improves the lamellipodial and invadopodial protrusions for driving cell migrations (Bera et al., 2022; Gong et al., 2021). Here, our above analysis shows how the mechanical forces (represented by the internal force  $t^*$ ) and the chemical reactions

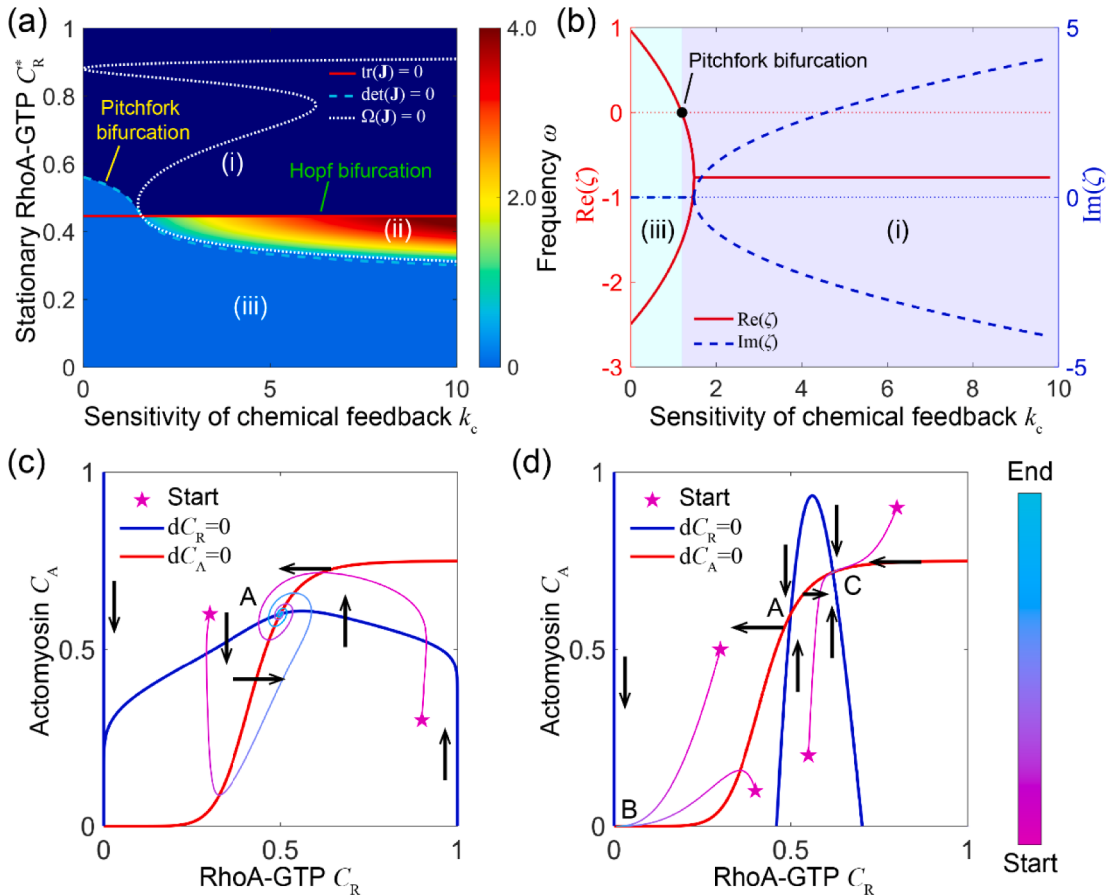


**Fig. 9.** Dynamics of an actomyosin string regulated by the chemical feedback. (a) The phase diagram regulated by the sensitivity of chemical feedback  $k_c$  and the stationary RhoA-GTP  $C_R^*$ . (b) The eigenvalues  $\zeta$  versus the sensitivity of chemical feedback  $k_c$ . The black point marks pitchfork bifurcation. The phase portraits with (c)  $k_c = 8$  and (d)  $k_c = 0.2$ . Several trajectories from different starts are plotted. The black arrows show the flow directions of pieces of nullclines. Through bifurcations, the stable fixed point A finally evolves into an unstable saddle, and two new stable fixed points B and C appear.

(represented by the stationary RhoA-GTP  $C_R^*$ ) jointly determine the dynamic stability of the stationary state in our model. The transition of dynamic state may provide a mechanism for the cytoskeleton to respond to biochemomechanical signals and execute cellular durotaxis and chemotaxis migrations.

## 5. Results and discussions

Using the tensegrity model of cytoskeletons in Section 2, we now perform numerical simulations to study the biochemomechanical evolutionary features of multiscale cytoskeleton structures. Two examples are provided. In the first, simulations of a string element comprising of actomyosin network are performed to show the typical evolutions of the three dynamic states and explore the effect of biochemomechanical feedback. In the second, the oscillatory patterns of a single cell are simulated to investigate the spontaneous dynamic cellular deformation and oscillation behaviors induced by the active contraction in the cytoskeleton.

### 5.1. Dynamic behaviors of an actomyosin string

In Section 4, we use the linear stability analysis method to analytically solve the dynamic states of a prestressed string regulated by the kinetic biochemomechanical signals. Here, we numerically simulate the dynamic evolution of variables and the trajectory in the variable phase plane. As shown in Fig. 8, the numerical variable evolutions and phase portraits demonstrate that the proposed biochemomechanical model can evolve into the three states:

- (i) *Stable State* (Fig. 8(a) and (b)): The two chemical fields will converge to the stationary state. In the phase plane, all trajectories that start near the target fixed point will approach it as  $t \rightarrow \infty$ . Fig. 8(b) shows the situation that the system settles down to equilibrium through damped oscillations, in which the trajectory decays each cycle along a spiral path.

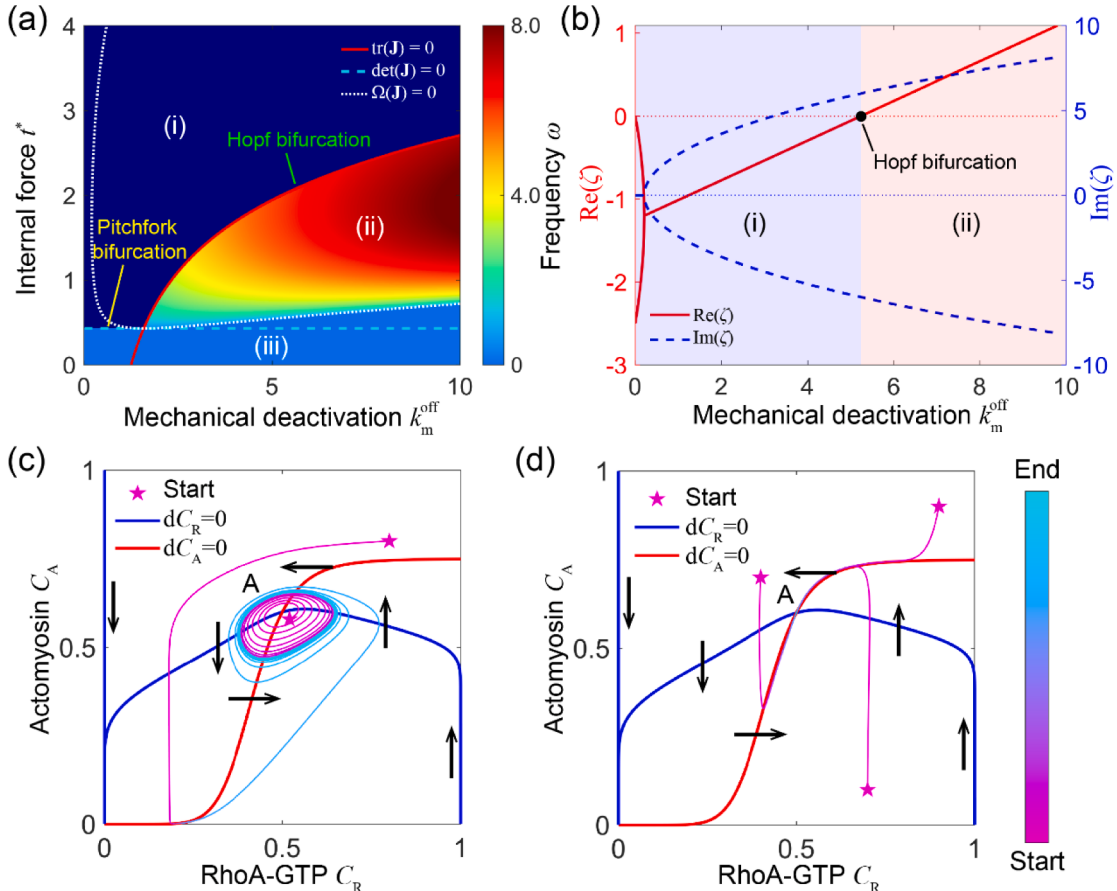


**Fig. 10.** Dynamics of an actomyosin string regulated by the mechanical feedback. (a) The phase diagram regulated by the internal force  $t^*$  and the mechanical deactivation  $k_m^{\text{off}}$ . (b) The eigenvalues  $\zeta$  versus the mechanical deactivation  $k_m^{\text{off}}$ . The black point marks Hopf bifurcation. The phase portraits with (c)  $k_m^{\text{off}} = 7$  and (d)  $k_m^{\text{off}} = 0.15$ . Through Hopf bifurcation, the limit cycle shrinks to zero amplitude and engulfs the fixed point A, rendering it stable.

- (ii) *Oscillatory State* (Fig. 8(c) and (d)): The two chemical fields will oscillate around the stationary state. In the phase plane, all trajectories will be attracted to a limit cycle as  $t \rightarrow \infty$ . In this situation, the system exhibits self-sustained and stable oscillations. If the system is perturbed slightly, it always returns to the standard cycle.
- (iii) *Unstable State* (Fig. 8(e) and (f)): The two chemical fields will collapse to an extreme value or another stationary state. In the phase plane, all trajectories will leave the target stationary state.

By decreasing the stationary RhoA-GTP  $C_R^*$ , the actomyosin string undergoes the transition from stable, to oscillatory, and then to unstable state. In addition, the simulations of our biochemomechanical model show that a limit cycle is born through Hopf bifurcation, and then the oscillatory state also arises spontaneously. The spontaneous shape oscillations are reported for both a single cell and collective cells in experimental observations (Salbreux et al., 2007; Solon et al., 2009). These robust oscillations, which can be sustained for several hours, participate in cytokinesis and cell locomotion or the stepwise tissue displacing and shaping during embryogenesis.

Combined with the linear stability analysis, we next explore how the biochemomechanical feedback affects the trajectory flow in the phase plane, changes the stability of the stationary state, and finally results in bifurcations. First, we examine the importance of chemical feedback that influences the mechanical properties of elements. Fig. 9(a) shows the phase diagram regulated by the sensitivity of chemical feedback  $k_c$  and the stationary RhoA-GTP  $C_R^*$ . When chemical feedback  $k_c$  is small, the oscillatory state (ii) vanishes. The decrease of  $k_c$  cannot change the trace of the Jacobi matrix  $\text{tr}(J)$  (red solid line in Fig. 9(a)), and thus the real part of two conjugate complex eigenvalues keeps constant (Fig. 9(b)). It indicates that Hopf bifurcation never happens as  $k_c$  is varied. In the case of two real eigenvalues, pitchfork bifurcation happens when an eigenvalue becomes positive. The flow of trajectories in the phase plane reflects the interesting influence of parameter changes. When chemical feedback  $k_c$  is large, all the trajectories flow around the fixed point A and converge to it gradually, forming a decaying spiral (Fig. 9(c)). When  $k_c$  decreases, the shape of the nullcline  $dC_R = 0$  becomes sharp, which may change the number of intersections of nullclines and result in the destructions, collisions, and creations of fixed points (Strogatz, 2018). Multiple zero-eigenvalue bifurcations make the original stable fixed point finally becomes a saddle (Fig. 9(d)). The flow of trajectories in the phase plane has changed qualitatively. In the cases that the stationary RhoA-GTP  $C_R^*$  is low (below the red solid line  $\text{tr}(J) = 0$  in Fig. 9(a)), the decrease of  $k_c$  destroys the limit cycle, and the original fixed point becomes first an unstable repeller and then a saddle.

Then, we examine the importance of mechanical feedback that influences the deactivation of RhoA-GTP. Fig. 10(a) shows the phase diagram regulated by the internal force  $t^*$  and the mechanical deactivation  $k_m^{\text{off}}$ . As in the case of chemical feedback, when mechanical feedback  $k_m^{\text{off}}$  is small, the oscillatory state (ii) vanishes. The decrease of  $k_m^{\text{off}}$  hardly changes the determinant of the Jacobi matrix  $\det(J)$ , but has a significant influence on its trace  $\text{tr}(J)$  (Fig. 10(a)). As  $k_m^{\text{off}}$  increases, the real part of two complex eigenvalues becomes positive, and Hopf bifurcation happens (Fig. 10(b)). In the phase plane with large  $k_m^{\text{off}}$ , trajectories converge to the limit cycle, away from the fixed point A or gather from the outside (Fig. 10(c)). When  $k_m^{\text{off}}$  decreases, the nullclines keep almost the same, but the amplitude of the limit cycle shrinks. In other words, the amplitude growth rate per cycle becomes slower and slower and finally changes to decay. A supercritical Hopf bifurcation happens, and the stationary state gains stability. When the mechanical deactivation  $k_m^{\text{off}}$  is extremely small, the biochemical fields in the element decay very fast, and the fixed point becomes an attractor (Fig. 10(d)). Throughout the process, the flow direction in the phase plane hardly changes.

In the above subsection, we have investigated the dynamic behaviors of a string that comprises a multi-scale actomyosin network. However, in a cellular tensegrity with multiple cytoskeletal elements, the cellular dynamic behaviors performing biological functions

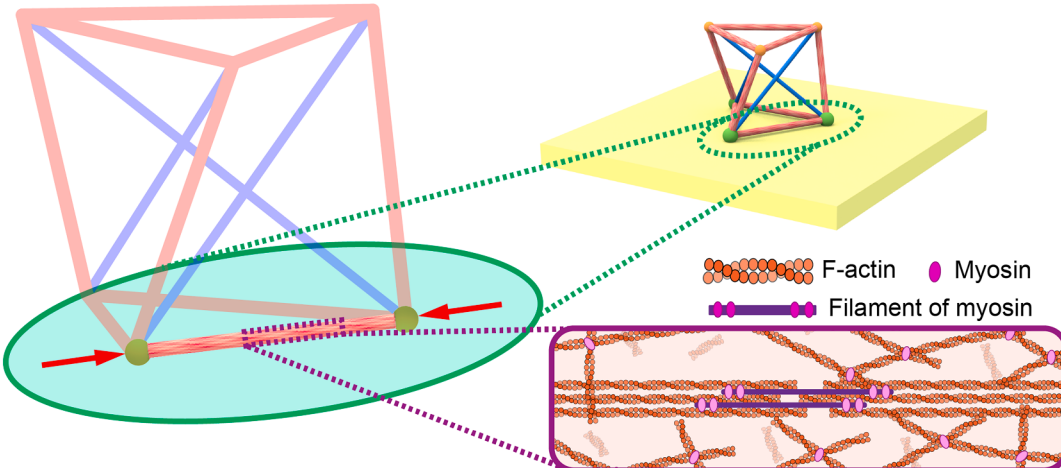


**Fig. 11.** Multiscale model of a non-adherent cell. The biochemomechanical signaling module coordinates the activity of myosin motors and the microscopic structure of cross-linked F-actins. This microscopic evolution endows the strings with active contraction and further contributes to the oscillatory patterns of the whole cellular structure.

are much more complex than that of an independent string. Especially, the internal force  $t^*$  of every cytoskeletal element relies on the overall mechanical equilibrium. The results of the prestressed string should be adapted when analyzing the parametric influences on the dynamics of the whole cellular structure. In what follows, numerical simulation is used to show the oscillation patterns of a complete cellular tensegrity structure.

### 5.2. Single-cell oscillation

Oscillations, which are widely observed in cells, play a significant role in their migrations, differentiations, and other dynamic processes. Here, we apply our biochemomechanical cellular tensegrity model to numerically investigate the single-cell spatiotemporal oscillation patterns and reveal their biophysical regulation mechanisms from the protein-protein interactions. A simplified tri-prism configuration, which still maintains the externally connected strings and the internal bars, is chosen to gain insights into the dynamic mechanisms of cell oscillation. As shown in Fig. 11, the cell is modeled as a tensegrity consisting of 9 strings and 3 bars, which represent the cortical actomyosin networks and microtubular networks, respectively. Salbreux et al. (2007) experimentally demonstrated spontaneous shape oscillations of 3T3 fibroblast cells occurred and lasted for hours at a constant frequency following a loss of cell–substrate adhesion. Hence, we only constrain the rigid-body displacement of the tensegrity to simulate the loss of cell–substrate adhesion. Simulations are performed in an initially mechanical self-equilibrium configuration of the tensegrity structure. The tensegrity has prestresses in its elements but is subjected to no external forces. As the cell size changes little during oscillation, we take the growth coefficient  $k_G = 0$  and the characteristic length  $l_c = 10 \mu\text{m}$ , which is the common radius of a cell.

Our model reproduced the shape oscillation of the single cell without any external influences, as shown in Fig. 12(a). After an initial fluctuation, both the chemical and mechanical variables of the cell spontaneously reach the dynamic equilibrium oscillatory states

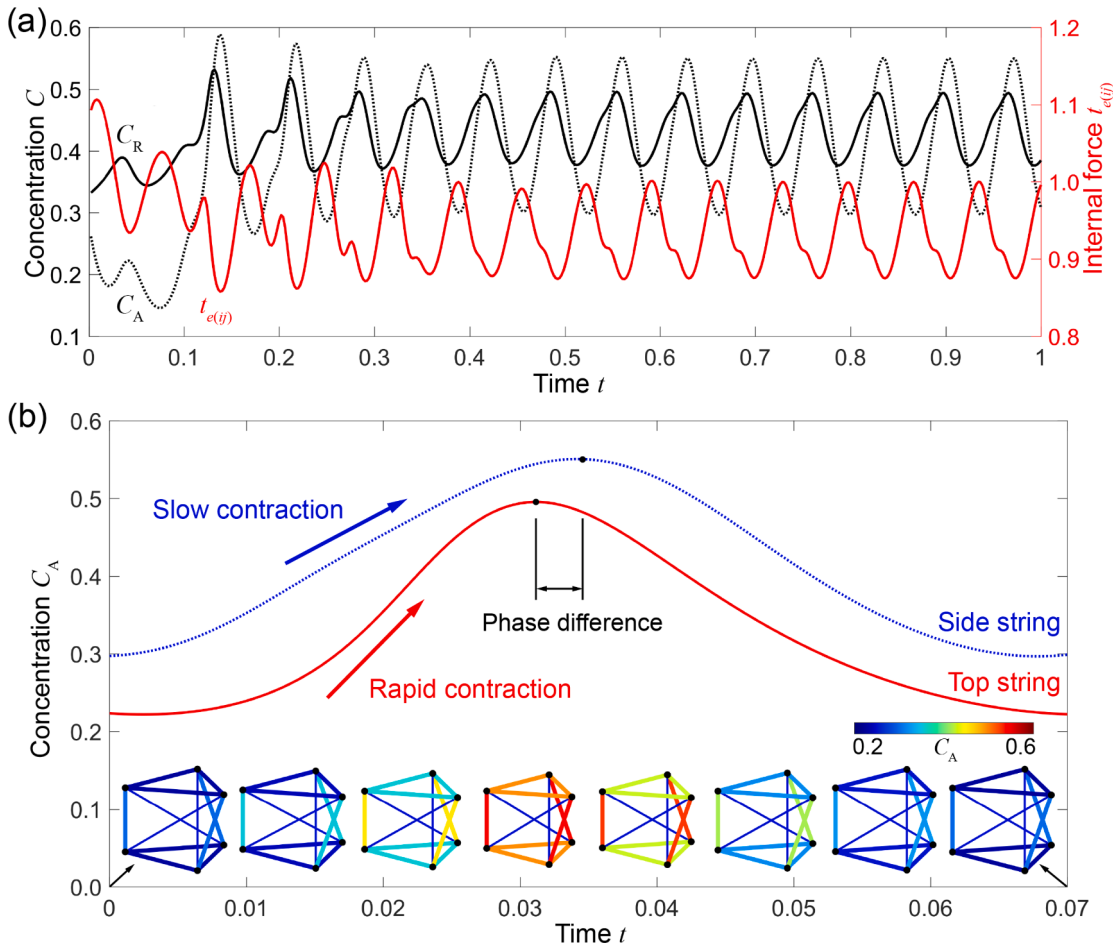


**Fig. 12.** Simulations of the oscillation of a cell. (a) Oscillations of RhoA-GTP concentration  $C_R$ , actomyosin concentration  $C_A$ , and internal force  $t_{e(ij)}$  in the side string of a tri-prism cell model. Here we take the parameters  $k_A^{\text{on}} = 1.5$ ,  $k_A^{\text{off}} = 0.5$ ,  $k_m^{\text{off}} = 1$ ,  $k_m = 14$ , and  $C_R^* = 0.38$ . (b) The shape oscillation of a tri-prism cell model in a cycle of the dynamic equilibrium state. All shapes are collected at an interval  $\Delta t = 0.01$ . The color of every string shows its actomyosin concentration  $C_A$ . There exists a phase difference between the oscillations of actomyosin concentration  $C_A$  in the side (blue dotted line) and top (red solid line) strings.

with the same frequency. However, there is a phase difference between the oscillations of actomyosin and RhoA-GTP. This phase difference shows that actomyosin is activated after RhoA-GTP with a time delay induced by the mechanosensitive pathway (Lin et al., 2017). Our simulations demonstrate that the oscillation of actomyosin through the chemical feedback directly influences the forces in the whole structure and thus leads to cell oscillations. At the dynamic equilibrium state, we get a cellular oscillatory period of  $0.0686t_c \approx 23$ s that agrees with the experimental measurement of 37s (Salbreux et al., 2007). Fig. 12(b) shows the cellular shape changes in each cycle of the dynamic equilibrium state. Our tensegrity model presents an overall oscillation, but there still exists slight differences between the side and top (both upper and lower) strings. A long and slow contraction occurs at the side strings, while a short and rapid contraction occurs at the top strings after an initial relaxation stage. This heterogeneous contraction causes a phase difference between the largest contractions of the side and top strings, and leads to anisotropic deformations of cells. The colors of strings show the activation level of actomyosin in regulating each deformed cell shape. The curves in Fig. 12(b) demonstrate that the top strings deform fast in  $t \in [0.02, 0.05]$ , and their actomyosin concentrations keep low values at other times. The side strings experience a more uniform deformation throughout the whole cycle.

### 5.3. Discussions

The above examples demonstrate that the present biochemomechanical model can reproduce the experimentally observed dynamic cellular deformation, chemical mass transport, and their interactions in the cytoskeleton at different length scales. In our model, the cell cortex with an abundant actomyosin network and microtubules are simplified as elastic strings and bars, respectively. Since RhoA-induced actin polymerization and myosin activation are the main driving forces for the active behaviors of cells, the effects of viscous cytoplasm have been ignored for simplicity. The analysis results reveal that the oscillatory state of cells occurs spontaneously because of the biochemomechanical coupling regulation of the cortical actomyosin network, without requiring any pre-assumed mechanical and chemical stimulations. It should be mentioned that the viscosity of cytoplasm may have a considerable influence on the oscillation pattern of cells (Lin et al., 2014). To more precisely investigate the oscillatory dynamics, therefore, it is necessary to incorporate the viscous dispersion of cytoplasm into the model in our future work.

By adjusting the characteristic length  $l_c$ , the characteristic time  $t_c = l_c^2 / D_R$ , and sensitivities of mechanical and chemical feedback,  $k_m$  and  $k_c$ , our results can be extended to structures at different length and time scales. The cortical actomyosin network contraction makes a dominant contribution to the population-level behaviors from embryo genetic perturbation (Chan et al., 2019; Song et al., 2022) to cancer cell invasion (Gong et al., 2021), so the present active tensegrity model can be applied to investigate multiscale cellular behaviors, such as the extension of cellular pseudopodia, the spreading and polarization of a single cell, and the migration of collective cells (Lv et al., 2021). It is worth mentioning that cellular motions can be driven by the propelling forces generated by polymerizing F-actin, such as lamellipodial and filopodial membrane protrusions and bacterial curved-path motions (Atilgan et al., 2006; Lin et al., 2010). By introducing specific molecular mechanisms, polymerization-based cellular motions can be simulated by the growth of rods or the active protrusion of nodes. Combined with an updated connection, the biochemomechanical tensegrity model can describe subcellular cytoskeletal structures with large topological changes, for example, nucleus deformation when passing through pores in ECMs (Venturini et al., 2020). In addition, during embryonic development, myosin-induced cortical contractions control the dynamics of cellular and nuclear size oscillations, and thus regulate the epigenetic states of cells (Chan et al., 2019). By considering the mechanical interactions between the microtubular network bar and nucleus, the present biochemomechanical tensegrity model can be further developed to investigate how myosin-induced cortical contractions impact the dynamic nuclear deformations.

## 6. Conclusions

In summary, we have established a biochemomechanical tensegrity model to describe the highly dynamic cytoskeletal structures and cell deformations. The coupling mechanisms of mechanical equilibrium, chemical reaction–diffusion, and their feedback are taken into account to reveal the active behaviors of the cytoskeleton, specifically, the generation of active contraction forces. The linear stability analysis of an actomyosin string shows that the active contraction forces positively contribute to the structural stability. The feedback mechanisms between active forces and chemical reactions result in a spontaneous oscillatory state, which is pivotal for embryonic development and cancer invasion. This model can simulate highly dynamic cellular processes at different timescales. Illustrative examples of dynamic behaviors of an actomyosin string and single-cell oscillation patterns are implemented. This work provides a tensegrity-based method that can not only describe biochemomechanical coupling processes of cytoskeletons but also model various dynamic cell functions derived from the kinetic interactions of molecular proteins.

Finally, it is pointed out that more realistic features of subcellular structures can be introduced further into our model. For example, the diffusion of biochemical factors greatly influences the dynamics of the system and leads to rich patterns in the physical space, such as Turing's patterns. Biological processes commonly show randomness, especially in the polymerization of actin networks and the establishment of cell–substrate adhesion, and greatly change the subsequent evolution of complex dynamic systems. In addition, the morphogenesis of cells also involves fluid transport and osmosis which have not been integrated into the present tensegrity model (Sun and Feng, 2022). These issues deserve further systematic investigations.

### Statement of Novelty

In this paper, we establish a biochemomechanical tensegrity model of cytoskeleton to investigate the spatiotemporal dynamics of

cells. It reveals that the interplay of internal active forces and chemical reactions may induce spontaneous oscillations of cells. To the best of our knowledge, no existing work has a significant overlap with this paper.

### Authorship contribution statement

**Shu-Yi Sun:** Established the theoretical model, Performed the linear stability analysis and simulations, Wrote the paper. **Li-Yuan Zhang:** Established the theoretical model, Wrote the paper. **Xindong Chen:** Wrote the paper. **Xi-Qiao Feng:** Conceived the problem, Designed the study, Wrote the paper.

### Author agreement

We confirm that this manuscript has been seen and approved by all authors, and our manuscript has not been published elsewhere and has been considered solely by your Journal.

### Declaration of Competing Interest

The authors declare that they have no known competing financial interests or personal relationships that could have appeared to influence the work reported in this paper.

### Data availability

Data will be made available on request.

### Acknowledgment

Supports from the National Natural Science Foundation of China (Grant Nos. 12032014 and 11921002) are acknowledged.

### References

- Adebawale, K., Gong, Z., Hou, J.C., Wisdom, K.M., Garbett, D., Lee, H., Nam, S., Meyer, T., Odde, D.J., Shenoy, V.B., Chaudhuri, O., 2021. Enhanced substrate stress relaxation promotes filopodia-mediated cell migration. *Nat. Mater.* 20, 1290–1299.
- Antonny, B., 2011. Mechanisms of membrane curvature sensing. *Annu. Rev. Biochem.* 80, 101–123.
- Atilgan, E., Wirtz, D., Sun, S.X., 2006. Mechanics and dynamics of actin-driven thin membrane protrusions. *Biophys. J.* 90, 65–76.
- Bement, W.M., Leda, M., Moe, Alison M., Kita, Angela M., Larson, Matthew E., Golding, Adriana E., Pfeuti, C., Su, K.-C., Miller, Ann L., Goryachev, Andrew B., von Dassow, G., 2015. Activator–inhibitor coupling between rho signalling and actin assembly makes the cell cortex an excitable medium. *Nat. Cell Biol.* 17, 1471–1483.
- Bera, K., Kiepas, A., Godet, I., Li, Y., Mehta, P., Ifemembu, B., Paul, C.D., Sen, A., Serra, S.A., Stoletov, K., Tao, J., Shatkin, G., Lee, S.J., Zhang, Y., Boen, A., Mistriiotis, P., Gilkes, D.M., Lewis, J.D., Fan, C.-M., Feinberg, A.P., Valverde, M.A., Sun, S.X., Konstantopoulos, K., 2022. Extracellular fluid viscosity enhances cell migration and cancer dissemination. *Nature* 611, 365–373.
- Besser, A., Schwarz, U.S., 2007. Coupling biochemistry and mechanics in cell adhesion: A model for inhomogeneous stress fiber contraction. *New J. Phys.* 9, 425.
- Bischof, J., Brand, C.A., Somogyi, K., Májer, I., Thome, S., Mori, M., Schwarz, U.S., Lénárt, P., 2017. A cdk1 gradient guides surface contraction waves in oocytes. *Nat. Commun.* 8, 849.
- Brangwynne, C.P., MacKintosh, F.C., Kumar, S., Geisse, N.A., Talbot, J., Mahadevan, L., Parker, K.K., Ingber, D.E., Weitz, D.A., 2006. Microtubules can bear enhanced compressive loads in living cells because of lateral reinforcement. *J. Cell Biol.* 173, 733–741.
- Chan, C.J., Costanzo, M., Ruiz-Herrero, T., Mönke, G., Petrie, R.J., Bergert, M., Díz-Muñoz, A., Mahadevan, L., Hiiragi, T., 2019. Hydraulic control of mammalian embryo size and cell fate. *Nature* 571, 112–116.
- Chen X.D., Zhu, H.X., Feng, X.-Q., Li, X.N., Lu, Y.T., Wang, Z.B., Rezgui, Y., 2020. Predictive assembling model reveals the self-adaptive elastic properties of lamellipodial actin networks for cell migration. *Commun. Biol.* 3, 616.
- Coughlin, M.F., Stamenović, D., 1998. A tensile model of the cytoskeleton in spread and round cells. *J. Biomech. Eng.-Trans. ASME* 120, 770–777.
- Dalheimer, P., Pollard, T.D., Nolen, B.J., 2008. Nucleotide-mediated conformational changes of monomeric actin and arp3 studied by molecular dynamics simulations. *J. Mol. Biol.* 376, 166–183.
- Dance, A., 2021. The secret forces that squeeze and pull life into shape. *Nature* 589, 186–188.
- Dawes, Adriana T., Munro, Edwin M., 2011. Par-3 oligomerization may provide an actin-independent mechanism to maintain distinct par protein domains in the early caenorhabditis elegans embryo. *Biophys. J.* 101, 1412–1422.
- Deshpande, V., Mrksich, M., McMeeking, R., Evans, A., 2008. A bio-mechanical model for coupling cell contractility with focal adhesion formation. *J. Mech. Phys. Solids* 56, 1484–1510.
- Deshpande, V.S., McMeeking, R.M., Evans, A.G., 2007. A model for the contractility of the cytoskeleton including the effects of stress-fibre formation and dissociation. *Proc. R. Soc. A-Math. Phys. Eng. Sci.* 463, 787–815.
- Fenix, A.M., Burnette, D.T., 2018. Nikon's small world photo competition: Image of distinction. <https://www.nikonsmallworld.com/galleries/2018-photomicrography-competition/mouse-embryonic-fibroblast-cell-stained-for-actin-magenta-golgi-orange-and-nucleus-blue> (accessed 23 September 2022).
- Ferreira, J.P.S., Parente, M.P.L., Jorge, R.M.N., 2018. Continuum mechanical model for cross-linked actin networks with contractile bundles. *J. Mech. Phys. Solids* 110, 100–117.
- Ferrell, James E., Tsai, Tony Y.-C., Yang, Q., 2011. Modeling the cell cycle: Why do certain circuits oscillate? *Cell* 144, 874–885.
- Fletcher, D.A., Mullins, R.D., 2010. Cell mechanics and the cytoskeleton. *Nature* 463, 485–492.
- Friedl, P., Gilmour, D., 2009. Collective cell migration in morphogenesis, regeneration and cancer. *Nat. Rev. Mol. Cell Biol.* 10, 445–457.
- Giannone, G., Dubin-Thaler, B.J., Döbereiner, H.-G., Kieffer, N., Bresnick, A.R., Sheetz, M.P., 2004. Periodic lamellipodial contractions correlate with rearward actin waves. *Cell* 116, 431–443.
- Gong, B., Wei, X., Qian, J., Lin, Y., 2019. Modeling and simulations of the dynamic behaviors of actin-based cytoskeletal networks. *ACS Biomater. Sci. Eng.* 5, 3720–3734.

- Gong, Z., Wisdom, K.M., McEvoy, E., Chang, J., Adebawale, K., Price, C.C., Chaudhuri, O., Shenoy, V.B., 2021. Recursive feedback between matrix dissipation and chemo-mechanical signaling drives oscillatory growth of cancer cell invadopodia. *Cell Reports* 35, 109047.
- Goriely, A., 2018. Five ways to model active processes in elastic solids: Active forces, active stresses, active strains, active fibers, and active metrics. *Mech. Res. Commun.* 93, 75–79.
- Gudipaty, S.A., Lindblom, J., Loftus, P.D., Redd, M.J., Edes, K., Davey, C.F., Krishnegowda, V., Rosenblatt, J., 2017. Mechanical stretch triggers rapid epithelial cell division through piezo1. *Nature* 543, 118–121.
- Guest, S.D., 2010. The stiffness of tensegrity structures. *IMA J. Appl. Math.* 76, 57–66.
- Hannezo, E., Prost, J., Joanny, J.-F., 2014. Theory of epithelial sheet morphology in three dimensions. *Proc. Natl. Acad. Sci. U. S. A.* 111, 27–32.
- Huber, F., Schnauss, J., Ronicke, S., Rauch, P., Muller, K., Futterer, C., Kas, J., 2013. Emergent complexity of the cytoskeleton: From single filaments to tissue. *Adv. Phys.* 62, 1–112.
- Huber, L., Suzuki, R., Krüger, T., Frey, E., Bausch, A.R., 2018. Emergence of coexisting ordered states in active matter systems. *Science* 361, 255–258.
- Imtiaz, M.S., Katnik, C.P., Smith, D.W., van Helden, D.F., 2006. Role of voltage-dependent modulation of store  $Ca^{2+}$  release in synchronization of  $Ca^{2+}$  oscillations. *Biophys. J.* 90, 1–23.
- Inagaki, N., Katsuno, H., 2017. Actin waves: Origin of cell polarization and migration? *Trends Cell Biol.* 27, 515–526.
- Ingber, D.E., 2018. From mechanobiology to developmentally inspired engineering. *Trans. R. Soc. B-Biol. Sci.* 373, 20170323.
- Ingber, D.E., Wang, N., Stamenović, D., 2014. Tensegrity, cellular biophysics, and the mechanics of living systems. *Rep. Prog. Phys.* 77, 046603.
- Janmey, P.A., McCulloch, C.A., 2007. Cell mechanics: Integrating cell responses to mechanical stimuli. *Annu. Rev. Biomed. Eng.* 9, 1–34.
- Koenderink, G.H., Paluch, E.K., 2018. Architecture shapes contractility in actomyosin networks. *Curr. Opin. Cell Biol.* 50, 79–85.
- Kumar, S., Maxwell, I.Z., Heisterkamp, A., Polte, T.R., Salanga, M., Mazur, E., Ingber, D.E., 2006. Viscoelastic retraction of single living stress fibers and its impact on cell shape, cytoskeletal organization, and extracellular matrix mechanics. *Biophys. J.* 90, 3762–3773.
- Lecuit, T., Lenne, P.-F., Munro, E., 2011. Force generation, transmission, and integration during cell and tissue morphogenesis. *Annu. Rev. Cell Dev. Biol.* 27, 157–184.
- Lee, H., Alisafaei, F., Adebawale, K., Chang, J., Shenoy, V.B., Chaudhuri, O., 2021. The nuclear piston activates mechanosensitive ion channels to generate cell migration paths in confining microenvironments. *Sci. Adv.* 7, eabd4058.
- Lessey, E.C., Guilluy, C., Burridge, K., 2012. From mechanical force to rhoa activation. *Biochemistry* 51, 7420–7432.
- Lin, S.-Z., Li, B., Lan, G., Feng, X.-Q., 2017. Activation and synchronization of the oscillatory morphodynamics in multicellular monolayer. *Proc. Natl. Acad. Sci. U. S. A.* 114, 8157–8162.
- Lin, S.-Z., Xue, S.-L., Li, B., Feng, X.-Q., 2018. An oscillating dynamic model of collective cells in a monolayer. *J. Mech. Phys. Solids* 112, 650–666.
- Lin, Y., Shenoy, V.B., Hu, B., Bai, L., 2010. A microscopic formulation for the actin-driven motion of listeria in curved paths. *Biophys. J.* 99, 1043–1052.
- Lin, Y., Wei, X., Qian, J., Sze, K.Y., Shenoy, V.B., 2014. A combined finite element-langevin dynamics (fem-ld) approach for analyzing the mechanical response of bio-polymer networks. *J. Mech. Phys. Solids* 62, 2–18.
- Liu, Y., Zhang, L.-Y., Wang, B.-C., Xu, G.-K., Feng, X.-Q., 2021. Why are isolated and collective cells greatly different in stiffness? *J. Mech. Phys. Solids* 147, 104280.
- Lomakin, A.J., Cattin, C.J., Cuvelier, D., Alraies, Z., Molina, M., Nader, G.P.F., Srivastava, N., Sáez, P.J., García-Arcos, J.M., Zhitnyak, I.Y., Bhargava, A., Driscoll, M. K., Welf, E.S., Fiolka, R., Petrie, R.J., De Silva, N.S., González-Granado, J.M., Manel, N., Lennon-Duménil, A.M., Müller, D.J., Piel, M., 2020. The nucleus acts as a ruler tailoring cell responses to spatial constraints. *Science* 370, eaba2894.
- Lopez-Menendez, H., Gonzalez-Torres, L., 2019. A theory to describe emergent properties of composite f-actin and vimentin networks. *J. Mech. Phys. Solids* 127, 208–220.
- Lv, J.-Q., Chen, P.-C., Guan, L.-Y., Gozdz, W.T., Feng, X.-Q., Li, B., 2021. Collective migrations in an epithelial–cancerous cell monolayer. *Acta Mech. Sin.* 37, 773–784.
- Marchetti, M.C., Joanny, J.F., Ramaswamy, S., Liverpool, T.B., Prost, J., Rao, M., Simha, R.A., 2013. Hydrodynamics of soft active matter. *Rev. Mod. Phys.* 85, 1143–1189.
- Miller, C.J., Davidson, L.A., 2013. The interplay between cell signalling and mechanics in developmental processes. *Nat. Rev. Genet.* 14, 733–744.
- Miller, P.W., Stoop, N., Dunkel, J., 2018. Geometry of wave propagation on active deformable surfaces. *Phys. Rev. Lett.* 120, 268001.
- Mueller, J., Szep, G., Nemethova, M., de Vries, I., Lieber, A.D., Winkler, C., Kruse, K., Small, J.V., Schmeiser, C., Keren, K., Hauschild, R., Sixt, M., 2017. Load adaptation of lamellipodial actin networks. *Cell* 171, 188–200.
- Munjal, A., Philippe, J.-M., Munro, E., Lecuit, T., 2015. A self-organized biomechanical network drives shape changes during tissue morphogenesis. *Nature* 524, 351–355.
- Murrell, M., Oakes, P.W., Lenz, M., Gardel, M.L., 2015. Forcing cells into shape: The mechanics of actomyosin contractility. *Nat. Rev. Mol. Cell Biol.* 16, 486–498.
- Murtada, S.-I., Kroon, M., Holzapfel, G.A., 2010. A calcium-driven mechanochemical model for prediction of force generation in smooth muscle. *Biomech. Model. Mechanobiol.* 9, 749–762.
- Recho, P., Hallou, A., Hannezo, E., 2019. Theory of mechanochemical patterning in biphasic biological tissues. *Proc. Natl. Acad. Sci. U. S. A.* 116, 5344–5349.
- Reversat, A., Gaertner, F., Merrin, J., Stopp, J., Tasciyan, S., Aguilera, J., de Vries, I., Hauschild, R., Hons, M., Piel, M., Callan-Jones, A., Voituriez, R., Sixt, M., 2020. Cellular locomotion using environmental topography. *Nature* 582, 582–585.
- Salbreux, G., Joanny, J.F., Prost, J., Pullarkat, P., 2007. Shape oscillations of non-adhering fibroblast cells. *Phys. Biol.* 4, 268–284.
- Salbreux, G., Jülicher, F., 2017. Mechanics of active surfaces. *Phys. Rev. E* 96, 032404.
- Sedzinski, J., Biro, M., Oswald, A., Tinevez, J.-Y., Salbreux, G., Paluch, E., 2011. Polar actomyosin contractility destabilizes the position of the cytokinetic furrow. *Nature* 476, 462–466.
- Shao, D.Y., Levine, H., Rappel, W.J., 2012. Coupling actin flow, adhesion, and morphology in a computational cell motility model. *Proc. Natl. Acad. Sci. U. S. A.* 109, 6851–6856.
- Shenoy, V.B., Wang, H.L., Wang, X., 2016. A chemo-mechanical free-energy-based approach to model durotaxis and extracellular stiffness-dependent contraction and polarization of cells. *Interface Focus* 6, 20150067.
- Solon, J., Kaya-Cöpür, A., Colombelli, J., Brunner, D., 2009. Pulsed forces timed by a ratchet-like mechanism drive directed tissue movement during dorsal closure. *Cell* 137, 1331–1342.
- Song, Y., Soto, J., Chen, B., Hoffman, T., Zhao, W., Zhu, N., Peng, Q., Liu, L., Ly, C., Wong, P.K., Wang, Y., Rowat, A.C., Kurdistani, S.K., Li, S., 2022. Transient nuclear deformation primes epigenetic state and promotes cell reprogramming. *Nat. Mater.* 21, 1191–1199.
- Strogatz, S.H., 2018. Nonlinear dynamics and chaos with student solutions manual: With applications to physics, biology, chemistry, and engineering, Second Edition ed. CRC Press, Boca Raton, Florida.
- Sun, S.-Y., Feng, X.-Q., 2022. Fluid–solid coupling dynamic model for oscillatory growth of multicellular lumens. *J. Biomech.* 131, 110937.
- Sun, S.Y., Zhang, H., Fang, W., Chen, X., Li, B., Feng, X.-Q., 2022. Chapter three - bio-chemo-mechanical coupling models of soft biological materials: A review. In: Bordas, S.P.A. (Ed.), Chapter three - bio-chemo-mechanical coupling models of soft biological materials: A review. *Adv. Appl. Mech.* 55, 309–392.
- Sunyer, R., Trepat, X., 2020. Durotaxis. *Curr. Biol.* 30, R383–R387.
- Théry, M., 2010. Micropatterning as a tool to decipher cell morphogenesis and functions. *J. Cell Sci.* 123, 4201–4213.
- Valet, M., Siggia, E.D., Brivanlou, A.H., 2022. Mechanical regulation of early vertebrate embryogenesis. *Nat. Rev. Mol. Cell Biol.* 23, 169–184.
- Van Haastert, P.J.M., Devreotes, P.N., 2004. Chemotaxis: Signalling the way forward. *Nat. Rev. Mol. Cell Biol.* 5, 626–634.
- Venturini, V., Pezzano, F., Català Castro, F., Häkkinen, H.-M., Jiménez-Delgado, S., Colomer-Rosell, M., Marro, M., Tolosa-Ramon, Q., Paz-López, S., Valverde, M.A., Weghuber, J., Loza-Alvarez, P., Krieg, M., Wieser, S., Ruprecht, V., 2020. The nucleus measures shape changes for cellular proprioception to control dynamic cell behavior. *Science* 370, eaba2644.
- Wang, B.-C., Xu, G.-K., 2022. Cell chirality regulates coherent angular motion on small circular substrates. *Biophys. J.* 121, 1931–1939.
- Wang, N., Butler, J.P., Ingber, D.E., 1993. Mechanotransduction across the cell surface and through the cytoskeleton. *Science* 260, 1124–1127.

- Wang, N., Naruse, K., Stamenović, D., Fredberg, J.J., Mijailovich, S.M., Tolić-Nørrelykke, I.M., Polte, T., Mannix, R., Ingber, D.E., 2001. Mechanical behavior in living cells consistent with the tensegrity model. *Proc. Natl. Acad. Sci. U. S. A.* 98, 7765–7770.
- Wang, N., Tytell, J.D., Ingber, D.E., 2009. Mechanotransduction at a distance: Mechanically coupling the extracellular matrix with the nucleus. *Nat. Rev. Mol. Cell Biol.* 10, 75–82.
- Wang, T., Hamilla, S., Cam, M., Aranda-Espinoza, H., Mili, S., 2017. Extracellular matrix stiffness and cell contractility control rna localization to promote cell migration. *Nat. Commun.* 8, 896.
- Wang, X.B., Zhu, H.X., Lu, Y.T., Wang, Z.B., Kennedy, D., 2020. The elastic properties and deformation mechanisms of actin filament networks crosslinked by filamins. *J. Mech. Behav. Biomed. Mater.* 112, 104075.
- Xu, G.-K., Feng, X.-Q., Gao, H., 2018. Orientations of cells on compliant substrates under biaxial stretches: A theoretical study. *Biophys. J.* 114, 701–710.
- Yang, W., Luo, M., Gao, Y., Feng, X.-Q., Chen, J., 2023. Mechanosensing model of fibroblast cells adhered on a substrate with varying stiffness and thickness. *J. Mech. Phys. Solids* 171, 105137.
- Yin, S., Li, B., Feng, X.-Q., 2021. Bio-chemo-mechanical theory of active shells. *J. Mech. Phys. Solids* 152, 104419.
- Yin, S., Li, B., Feng, X.-Q., 2022. Three-dimensional chiral morphodynamics of chemomechanical active shells. *Proc. Natl. Acad. Sci. U. S. A.* 119, e2206159119.
- Zhang, J., Guo, W.-H., Wang, Y.-L., 2014a. Microtubules stabilize cell polarity by localizing rear signals. *Proc. Natl. Acad. Sci. U. S. A.* 111, 16383–16388.
- Zhang, L.-Y., Li, Y., Cao, Y.-P., Feng, X.-Q., 2014b. Stiffness matrix based form-finding method of tensegrity structures. *Eng. Struct.* 58, 36–48.
- Zhang, L.-Y., Li, Y., Cao, Y.-P., Feng, X.-Q., Gao, H., 2013. A numerical method for simulating nonlinear mechanical responses of tensegrity structures under large deformations. *J. Appl. Mech.-Trans. ASME* 80, 061018.
- Zhang, L., Feng, X.-Q., Li, S., 2017. Review and perspective on soft matter modeling in cellular mechanobiology: Cell contact, adhesion, mechanosensing, and motility. *Acta Mech* 228, 4095–4122.